**Article:**
Silva, D, Piazolo, S, Daczko, NR et al. (2018) Intracontinental Orogeny Enhanced by Far-field Extension and Local Weak Crust. Tectonics, 37 (12). pp. 4421-4443. ISSN: 0278-7407

https://doi.org/10.1029/2018TC005106

AGU100 ADVANCING EARTH AND SPACE SCIENCE

Tectonics

RESEARCH ARTICLE
10.1029/2018TC005106

Special Section:
An appraisal of Global Continental Crust: Structure and Evolution

# Intracontinental Orogeny Enhanced by Far-Field Extension and Local Weak Crust

**David Silva[1], Sandra Piazolo[1,2], Nathan R. Daczko[1], Gregory Houseman[2], Tom Raimondo[3,4], and Lynn Evans[5]**

[1]ARC Centre of Excellence for Core to Crust Fluid Systems and GEMOC, Department of Earth and Planetary Sciences, Macquarie University, Sydney, New South Wales, Australia, [2]School of Earth and Environment, Institute of Geophysics and Tectonics, University of Leeds, Leeds, UK, [3]School of Natural and Built Environments, University of South Australia, Adelaide, South Australia, Australia, [4]Future Industries Institute, University of South Australia, Adelaide, South Australia, Australia, [5]School of Earth, Atmosphere and Environmental Sciences, Monash University, Clayton, Victoria, Australia

**Abstract** The accommodation of intraplate stresses in preexisting weak regions of plate interiors is here investigated using thin viscous sheet numerical models. The intraplate stresses are governed by multicomponent and multidirectional stresses originating at plate boundaries. The modeled scenarios mimic plate boundary conditions during the intraplate Alice Springs Orogeny (ASO), central Australia, and include (1) a northwest-southeast zone of weak lithosphere within strong continental blocks to the north and southand (2) a principal south directed stress condition at the northern boundary that causes minor clockwise rotation of the northern block. Alternative tectonic environments are investigated in additional models that include (1) secondary compressional or extensional stresses acting at the eastern boundary, representing the temporally variable stress conditions during the Tasmanides Orogeny, and (2) an eastern wedge-shaped zone of rheologically weak lithosphere, mirroring rift fill of the Irindina subbasin. Our results highlight that a low angle between major crustal features (e.g., orogenic elongation and preexisting regional structures) and the principal transmitted stresses is highly relevant in the concentration of elevated levels of differential stress and subsequent localization of deformation in plate interiors. Secondary stresses orthogonal to the principal acting stresses may introduce effects that explain the episodic orogenic activity in the case of the ASO. The combination of secondary extensional stresses at the eastern boundary of Australia and weak lithosphere of the preexisting Irindina subbasin strongly influences the observed spatial strain intensity, localization, and kinematics of deformation during the ASO.

**Key Points:**
- We investigated the intracontinental orogeny enabled by preexisting intraplate crustal zones of weakness at low angle to subsequent principal stresses
- Secondary stresses, orthogonal to the principal stress, are important in the episodic development and evolution of intracontinental orogeny
- Extensional secondary stresses enhance the lateral extrusion of lower crustal material from weak areas

**Supporting Information:**
- Supporting Information S1

**Correspondence to:**
D. Silva,
david.barbosa-da-silva@hdr.mq.edu.au

**Citation:**
Silva, D., Piazolo, S., Daczko, N. R., Houseman, G., Raimondo, T., & Evans, L. (2018). Intracontinental orogeny enhanced by far-field extension and local weak crust. *Tectonics*, *37*. https://doi.org/10.1029/2018TC005106

Received 17 APR 2018
Accepted 23 OCT 2018
Accepted article online 9 NOV 2018



## 1. Introduction

The theory of plate tectonics has, since its emergence in the 1960s, provided a remarkably coherent framework to explain the majority of large-scale geological features observable at the Earth's surface, including mountain belts, rift valleys, and volcanic chains. One of the cornerstones of the plate tectonics theory is the assumption that plate boundaries are the main loci of tectonic stresses that drive the formation of large-scale geological features. Accordingly, it predicts that mountain belts are formed at plate boundaries. Intracontinental compressional orogens, however, which are distinct from conventional compressional orogens by their location within plate interiors, do not follow this fundamental rule (Cunningham, 2005; Raimondo et al., 2014). In contrast, they represent major zones of strain localization associated with crustal thickening and deep exhumation of basement rocks distal from active plate boundaries (Cunningham, 2005; Hand & Sandiford, 1999; Raimondo et al., 2010; Sandiford et al., 2001). As such, understanding the underlying causes and processes enabling intracontinental orogeny is one of the remaining gaps in our knowledge of the fundamental workings of the Earth.

The Neoproterozoic Petermann and Paleozoic Alice Springs Orogens of central Australia are primary examples of ancient intracontinental orogenesis that have been extensively studied in recent years (e.g., Aitken et al., 2009; Camacho & McDougall, 2000; Hand & Sandiford, 1999; McLaren et al., 2009; Raimondo et al., 2014, and references therein). Currently, intracontinental orogenesis is recognized in several parts of the world, such as central Asia (Tien Shan and Altai Orogens; Cunningham, 2005; Molnar & Tapponnier, 1975), South America (Borborema Province; Neves, 2003; Tommasi et al., 1995), North America (Sevier-Laramide Orogen and Kapuskasing uplift; Livaccari, 1991; Marshak et al., 2000; Perry et al., 2006), Iberia (Spanish Central System; Andeweg et al., 1999), and Africa (Atlas Mountains and Damara Belt; Kröner, 1977;

Ramdani, 1998; Teixell et al., 2003). Just like their plate boundary counterparts, these orogens involve crustal thickening coupled with topographic highs, exhumation of high-grade metamorphic rocks, localized melting and magmatism, and enhanced erosion feeding sediments into deep basins at the orogenic front(s).

Details of the underlying causes of intracontinental orogenesis are a matter of ongoing debate. In contrast to mountain belts developed at plate boundaries, intracontinental orogens require a stress component locally derived in the intraplate region by deep lithospheric instabilities (e.g., upper mantle gravitational [Rayleigh-Taylor] instabilities; Gorczyk et al., 2013; Gorczyk & Vogt, 2015; Neil & Houseman, 1999; Pysklywec & Beaumont, 2004) or by transmission of horizontal forces by strong lithosphere into plate interiors (Handy & Brun, 2004; Roberts & Houseman, 2001; Shaw et al., 1991). As an example, the loci of stress production that caused orogenesis in central Australia (e.g., Peterman and Alice Springs Orogens) are debated as being driven by either proximal intraplate stress or distal plate boundary stresses (see Raimondo et al., 2014, for a comprehensive review). In the case of the Alice Springs Orogeny (ASO), the argument for transmission of plate boundary stresses is evidenced by the complementary tectonic evolution of the accretionary Tasman Orogenic System (Champion et al., 2009; Collins, 2002; Glen, 2013; Gray & Foster, 2004; Raimondo et al., 2014). While geophysical and geological data show that many intraplate regions are under compressional stress regimes originating from far-field stresses (Coblentz et al., 1998; Hurd & Zoback, 2012; Zoback et al., 1989), intracontinental orogens are surprisingly rare when compared to their peri-plate located orogen counterparts; hence, the presence of zones of mechanical weakness in plate interiors must be one of the principal requirements to allow intraplate orogenesis. The seismological impact of active intracontinental orogens is closely related to stress transmission and stress accommodation in the lithosphere (Thomas & Powell, 2017); consequently, in-depth studies of this special class of orogen are needed to better understand the relevance of plate boundary stress conditions to intracontinental orogenic activity.

In summary, one class of intracontinental orogeny requires (1) far-field stresses transmitted through relatively strong plate margins and (2) a rheologically weak plate interior. The magnitude and direction of far-field stresses are directly related to the plate boundary configuration and the efficiency of lithospheric stress transfer (e.g., Roberts & Houseman, 2001). Previous numerical models focused their simulations on some or all of the aforementioned requirements, using inherited crustal structures of contrasting competence (e.g., Braun & Shaw, 2001; Heron & Pysklywec, 2016), lithospheric buckling instabilities (e.g., Regenauer-Lieb et al., 2015), or upper mantle gravitational Rayleigh-Taylor instabilities (e.g., Gorczyk et al., 2013; Gorczyk & Vogt, 2015; Neil & Houseman, 1999) to explain the observed spatio-temporal tectonic evolution of the central Australian region. The current debate therefore focuses on the nature of the far-field stresses (orientation and magnitude through time), the transmission of these stresses from plate boundaries to plate interiors, and the localization, orientation, structural architecture, and kinematics of orogenic activity.

Klootwijk (2013) highlights that both primary collisional forces at plate boundaries (i.e., forces acting near perpendicular to orogen strike) and secondary plate boundary forces (i.e., forces contributing to the shear and normal traction acting at a low angle relative to the orogen strike) govern the character of intracontinental orogens. Proposed zones of weakness present in plate interiors include (1) old regional sutures (Braun & Shaw, 2001; Heron et al., 2016; Sandiford & Hand, 1998); (2) thermally weakened areas due to either sedimentary blanketing of high heat-producing crust or the upwelling of hot uppermost lithospheric mantle into the lower crust (Cunningham, 2013; Sandiford & Hand, 1998; Shaw et al., 1991; Walter et al., 1995), a variant of the latter being Rayleigh-Taylor gravitational instabilities (Gorczyk et al., 2013; Gorczyk & Vogt, 2015; Neil & Houseman, 1999); (3) a preexisting network of metasomatized midcrustal shear zones (Cartwright & Buick, 1999; Raimondo et al., 2011, 2013); and (4) deep sedimentary basins (Haines et al., 2001; Klootwijk, 2013). Depending on the rheological model of the lithosphere and geothermal gradient used (Burov & Watts, 2006), increased crustal thickness may decrease the strength of the lithosphere, owing to greater resistance of mantle rocks to deformation compared to the quartzo-feldspatic crust (Kusznir & Park, 1987; Ranalli & Murphy, 1987); although, decreasing thickness can increase or decrease its strength, depending on the strain rate (i.e., fast strain rate = strain softening and slow strain rate = strain hardening; Kusznir & Park, 1987).

In order to investigate the underlying causes of intracontinental orogeny, we numerically explore simple first-order rheological models the importance of (1) the geometry of intracontinental weak zones and (2) secondary plate boundary stresses. To constrain our model setup and compare model results to a real geological scenario, we utilize data from the long-lived (450–300 Ma) ASO in central Australia (Buick et al., 2008;

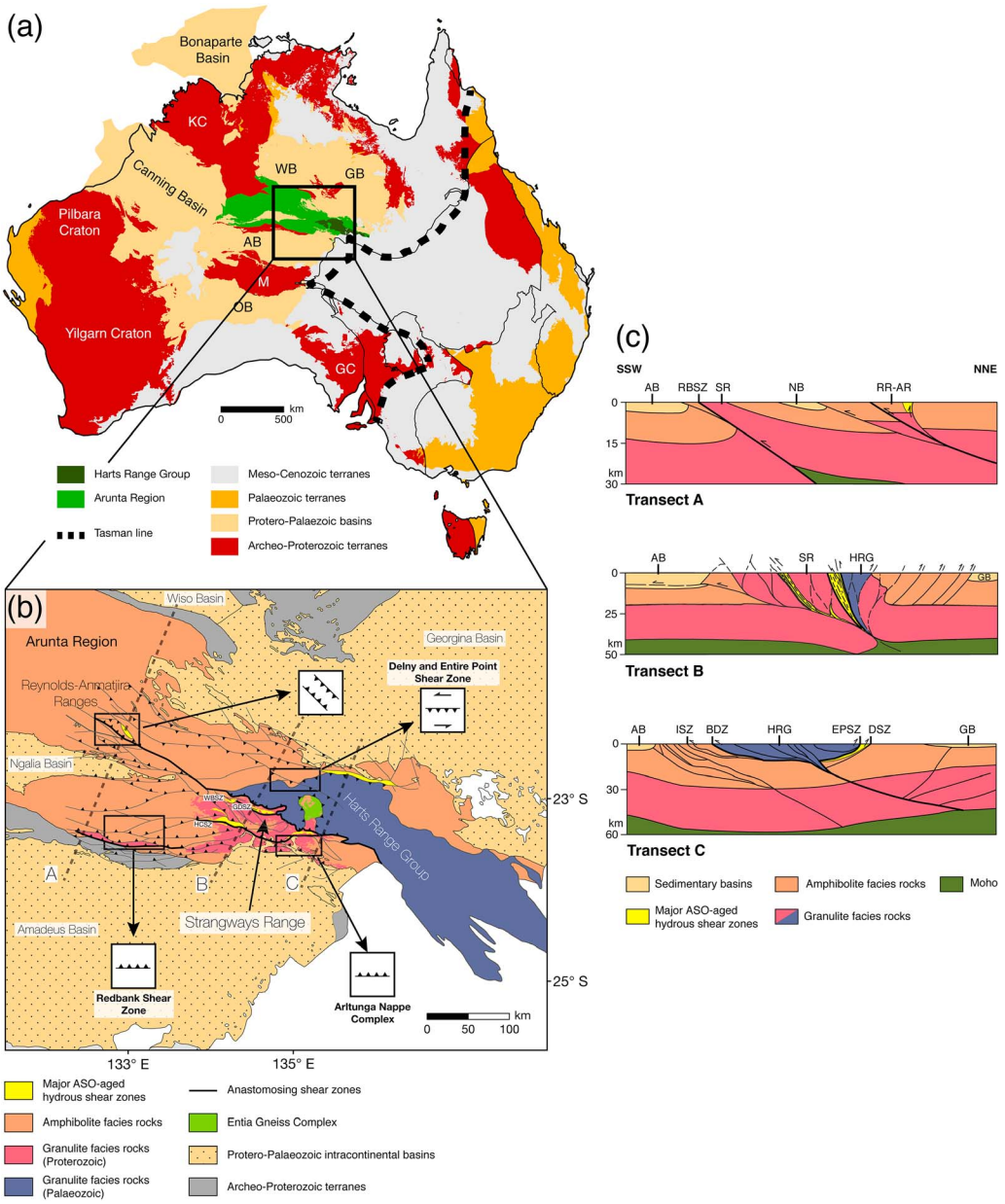


**Figure 1.** Geologic characteristics of the Alice Springs Orogeny and its regional context. (a) Generalized geologic map of the Australian continent, showing the major tectonic subdivisions, the location of the Arunta Region, and position of Transects A–C (modified after Raimondo et al., 2014). (b) Regional geologic map of the SE Arunta Region, emphasizing the distribution of granulite and amphibolite facies basement rocks and the location of the Reynolds-Anmatjira Ranges, Strangways Range, and the Harts Range in relation to major faults and hydrous shear zones (modified after Ballèvre et al., 2000; Collins & Teyssier, 1989; Maidment, 2005; Raimondo et al., 2011; Scrimgeour, 2013). (c) Simplified structural cross sections from Transect A (modified after Raimondo et al., 2014), Transect B (modified after Ballèvre et al., 2000; Collins & Teyssier, 1989), and Transect C (modified after Maidment et al., 2013), showing the differential exhumation patterns and structural architecture along strike of the Alice Springs Orogen. Abbreviations: AB, Amadeus Basin; AR, Anmatjira Range; BDZ, Bruna Detachment Zone; DSZ, Delny Shear Zone; EPSZ, Entire Point Shear Zone; GB, Georgina Basin; GC, Gawler Craton; GDSZ, Gough Dam Shear Zone; HCSZ, Harry Creek Shear Zone; HRG, Harts Range Group; ISZ, Illogwa Shear Zone; KC, Kimberley Craton; M, Musgrave Province; NB, Ngalia Basin; OB, Officer Basin; RBSZ, Redbank Shear Zone; RR, Reynolds Range; SR, Strangways Range; WBSZ, West Bore Shear Zone; WB, Wiso Basin.

Haines et al., 2001; Mawby et al., 1999), situated at the center of the Australian plate. The ASO is an ideal case study because it is one of the few intracontinental orogens that is now deeply exhumed, with midcrustal to lower crustal rocks exposed over several hundred kilometers of outcrop (Figure 1). Furthermore, the ASO has

a strongly episodic pattern of orogenic activity that is difficult to reconcile with current models of its formation (Raimondo et al., 2014).

We present results from numerical modeling extending the previous model of Roberts and Houseman (2001) that implemented far-field compressional stresses transmitted from the northern plate boundary to induce crustal thickening in a broad preexisting weak zone at the plate center. In contrast to this existing model that allowed a free secondary boundary to the east, our model adds another layer of complexity with either (1) compressional or (2) extensional stresses along the eastern boundary. Furthermore, we explore not only the effect of a pronounced preexisting weak zone oriented E-W that follows the pre-ASO Larapinta Rift (Klootwijk, 2013; Maidment, 2005) but also the existence of an eastern weak wedge. The latter is inspired by the recent recognition of an asymmetric bivergent subbasin rift represented by the ~35-km deep Harts Range Group (HRG) of the Irindina Province (Maidment, 2005; Tucker et al., 2015).

In the following, we first present a summary of the geological characteristics of the ASO, including the configuration of the Australian plate during the Paleozoic and the timing of plate movement, magmatism, metamorphism, deformation, and synorogenic sedimentation. This is followed by the general model setup, description of the models tested, and model analysis where numerical results are presented and discussed in the light of features specific to the ASO and to intracontinental orogenesis in general.

## 2. The Paleozoic ASO: A Deeply Exhumed Example of Intracontinental Mountain Building

### 2.1. General Geological Background and Structural Architecture

The ASO was a long-lived intracontinental mountain building event during the Ordovician to Carboniferous (450–300 Ma; Collins & Teyssier, 1989; Hand & Sandiford, 1999; Mawby et al., 1999). It is expressed in the Arunta Region of central Australia as a roughly E-W trending, ~700-km-long orogenic belt (Figure 1) characterized by an extensive regional network of anastomosing shear zones and thrust faults (Ballèvre et al., 2000; Cartwright et al., 1999; Raimondo et al., 2011, 2014). The width of the orogen varies from ~300 km in the west to ~80 km in the east. The eastern Alice Springs Orogen is characterized by crustal thickening and deep exhumation of ensialic granulitic basement rocks (Figure 1b), which from W to E are roughly constituted by the midcrustal Reynolds-Anmatjira Ranges, the midcrustal to deep-crustal Strangways Range and the deep-crustal Harts Range. The grade of metamorphism and pervasiveness of fluid hydration/retrogression of the granulitic basement increases from the 5–6 kbar and 500–600 °C in northwest (Reynolds-Anmatjira Ranges; Raimondo et al., 2011) to 10.5 kbar and 880 °C in the southeast (Harts Range; Mawby et al., 1999; Tucker et al., 2015).

The Reynolds-Anmatjira Ranges represent part of a tilted crustal-scale pop-up structure with the axial zone exhuming midcrustal granulites (Collins & Teyssier, 1989; Figures 1b and 1c). Discrete ASO-aged shear zones, up to 300 m wide, trend NW-SE and truncate Proterozoic folds and metamorphic fabrics (Cartwright & Buick, 1999; Collins & Teyssier, 1989; Raimondo et al., 2011). They exhibit north and south dipping foliations with dip-slip stretching lineations and a reverse sense of motion.

The Strangways Range represents a broad belt of granulite-facies basement up to ~125 km wide, formed as a consequence of the approximately 1,730-Ma Strangways Orogeny (Figures 1b and 1c). Multiple kilometer-scale shear zones dissect the terrane; these were reactivated during the ASO and include the West Bore and Gough Dam shear zones along its northern boundary and the Harry Creek Shear Zone at its southern boundary (Figure 1b). Together, the shear zones form a network of steeply dipping amphibolite- to greenschist-facies schist belts with south directed thrusting (Bendall, 2000; Ballèvre et al., 2000; Collins & Teyssier, 1989). The increase in shear zone width from the Reynolds-Anmatjira Ranges to the Strangways Range reflects a progressively deeper level of denudation (Raimondo et al., 2014).

The Harts Range is dominated by exposures of the HRG, a thick package of metabasic and amphibolite to granulite facies metasedimentary rocks contained in a roughly wedge-shaped area with a maximum width of ~150 km (Buick et al., 2005; Hand et al., 1999; Mawby et al., 1999; Figures 1b and 1c). Protoliths to the HRG were deposited in the Irindina subbasin, an asymmetrical bivergent rift formed toward the eastern plate margin during the approximately 520-Ma Stanovos Event. This rift is situated at the SE extremity of the Late Ordovician Larapinta seaway, an extensional corridor that cut diagonally across the Australian continent. The seaway

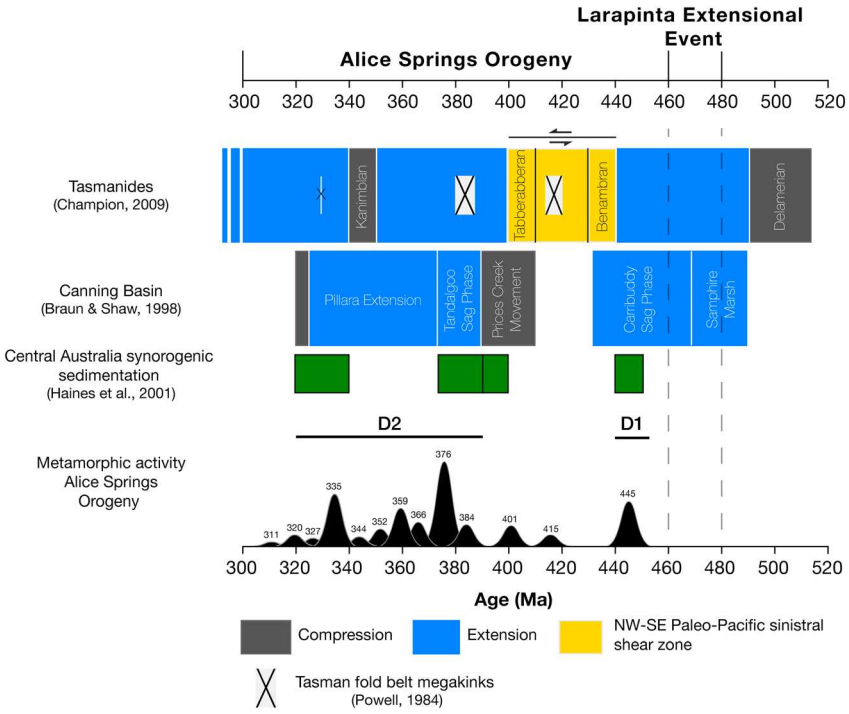


**Figure 2.** Sequential age comparison between metamorphic activity during the Alice Springs Orogeny (Gaussian deconvolution of frequency probability histogram; modified after Raimondo et al., 2014; Table S1) with the sequential Tasman Orogenic Belt (Tasmanides; Champion et al., 2009; Glen, 2013; Powell, 1984), the Canning Basin (Braun & Shaw, 1998), and the sedimentary record observed in synorogenic basins surrounding the Arunta Region (Haines et al., 2001). The timing of NW-SE sinistral shear between the Australian-Antarctic and Paleo-Pacific plates described by Gray and Foster (2004) is also shown (reconstruction in Figure 3a).

connected the depositional system of central Australia with the Canning Basin at the NW continental margin (Hand et al., 1999; Webby, 1978). It coincides with a continental-scale magnetic lineament suggesting a deep-seated structural discontinuity (Maidment, 2005; Myers et al., 1996; Shaw et al., 1995). The HRG was metamorphosed to granulite facies during the extensional Larapinta Event (480–460 Ma), as a consequence of high heat flow, mafic magmatism, and extremely deep burial to maximum depths of 30–35 km (Buick et al., 2001, 2005; Maidment, 2005; Maidment et al., 2013; Tucker et al., 2015). The western sector of the HRG is mostly constituted by the Irindina Gneiss, exhumed from 20- to 25-km depth during the ASO, and the mafic Meta-Igneous Complex intrusive rocks (emplacement at approximately 520 Ma; Maidment et al., 2013; Tucker et al., 2015).

From detailed structural mapping, Teyssier (1985) estimated that compression during the ASO resulted in shortening of up to 100 km in the eastern Arunta Region. The northern Arunta Region is characterized by dominantly coaxial deformation with upright and symmetrical reverse faults (Figures 1b and 1c). This coaxial movement is most pronounced in the NW sector, while a change to a noncoaxial sinistral kinematic regime is seen in the NE sector (Collins & Teyssier, 1989; Weisheit et al., 2016). Two of the most significant tectonic discontinuities are the Redbank Shear Zone and the Arltunga Nappe Complex. The Redbank Shear Zone consists of an ~400-km-long E-W trending zone of up to 10-km width. Thrust reactivation of this preexisting structure occurred at 450–420 Ma, displacing the Moho by up to 25 km (Biermeier et al., 2003; Wright et al., 1990). The Arltunga Nappe Complex separates the HRG from the underlying granulite facies rocks of the Strangways Range (Collins & Shaw, 1995; Figures 1b and 1c). The nappes extend E-W for ~100 km and probably involved piggyback imbrication on a regional scale, with significant crustal thickening of ~10 km constrained by K-feldspar, mica, and amphibole thermochronology (Dunlap et al., 1995).

### 2.2. Timing of Tectonic Evolution: ASO and Surrounding Tectonic Regions

In the following section, we summarize the main tectonic activity during the ASO (450–300 Ma; Figure 2) and place this activity in the context of coeval events within or at the margin of the Australian plate.

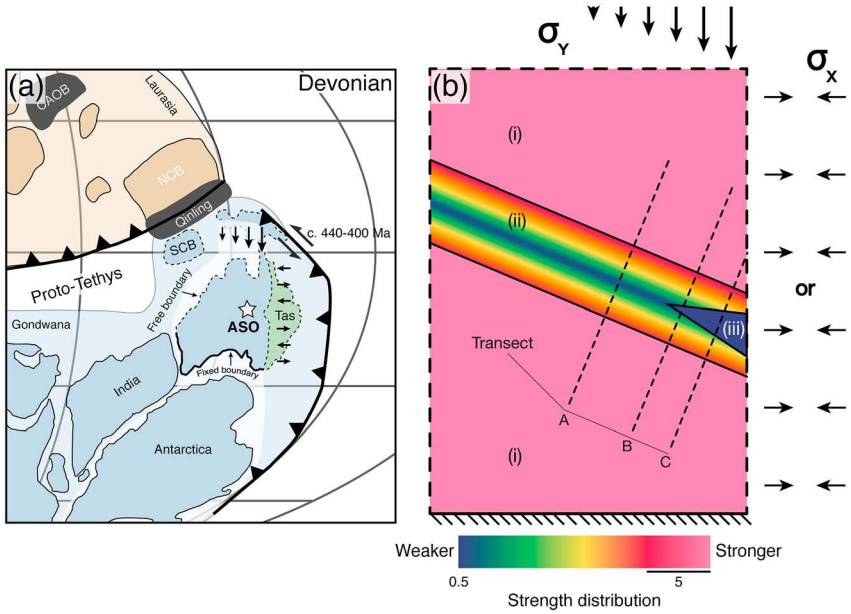


**Figure 3.** (a) Middle Devonian palaeogeographic reconstruction of the eastern collision between supercontinents Gondwana and Laurussia (future Laurasia; modified after Kröner et al., 2016). Palaeolatitudes are based on the palaeomagnetic model of Klootwijk (2010). Direction of the active stresses on the margin of the Australian continent is represented based on the aforementioned palaeogeographic reconstruction, the central Australian Alice Springs Orogeny (ASO), and the eastern Australian sequential Tasmanides (see Figure 2). Abbreviations: CAOB, Central Asia Orogenic Belt; NCB, North China Block; SCB, South China Block; Tas, Tasmanides. (b) Geometry of the numerical model, showing the active forces later applied in different simulation sets, and the geometry and strength distribution for each block inserted into the model (see explanatory details in section 3); (i) northern and southern strong blocks, (ii) diagonal weak band showing strength gradient from a relatively strong edge to weak center, and (iii) eastern weak wedge located within the weak band.

During the Ordovician-Carboniferous, the Australian plate was positioned within NE Gondwana. It was connected to the Antarctic and Indian plates to the south and southwest, bounded to the north by the North China Block, and to the east by the Tasmanides and a subduction zone involving westward subduction of the Pacific plate (Klootwijk, 2010; Figure 3a). The Tasmanides of eastern Australia show an early history (approximately 530 Ma) of westward advancing accretionary orogenesis, followed by ~2,000 km of eastward rollback migration of the subduction system, accompanied by back-arc extension and interspersed with Mid- to Late Paleozoic periods of advancing compressional orogenesis (Collins, 2002; Cawood et al., 2009; Champion et al., 2009; Glen, 2013; Figure 2).

The ASO immediately follows a pronounced extensional event at 480–460 Ma (the Larapinta Extensional Event; Buick et al., 2001, 2005), characterized by the opening of the Larapinta Rift and the deposition of protoliths to the HRG (Maidment et al., 2013). Inversion of the rift and compressional tectonics of the ASO initiated at approximately 450 Ma, with metamorphism first recognized at approximately 445 Ma (D1 period; Figure 2) and highly localized south directed reactivation of the Proterozoic Redbank Shear Zone at approximately 420 Ma (Biermeier et al., 2003; Figure 1b). This early activity in the ASO was contemporaneous with (1) extension and opening of the Canning Basin, Western Australia (Romine et al., 1994), and (2) collision between the Laurasian and Australian plates that began the Qinling Orogeny (Klootwijk, 2013; Meng & Zhang, 2000). At the same time, sediments were deposited in several large basins inside and outside the Arunta Region, including the Amadeus, Georgina, Wiso, and Ngalia Basins (Haines et al., 2001; Figures 1a and 1b).

A period of relative quiescence in the ASO persisted from 440–400 Ma. However, in the east, the Tasmanides experienced active E-W compression (the Benambran Orogeny at approximately 440 Ma and the Tabberabberan Orogeny at approximately 410 Ma; Champion et al., 2009), combined with N-S compression that formed the Tasman fold belt mega-kinks (i.e., a sharp change in tectonic grain orientation dated at approximately 415 Ma; Powell, 1984). During this time, NW-SE sinistral shear was active offshore the NE boundary between the Australian and Pacific plates (Gray & Foster, 2004; Figure 3a). The end of this period

(approximately 400 Ma) corresponds with the renewal of metamorphism and sediment deposition in the ASO (Haines et al., 2001).

The second major period of metamorphism during the ASO (D2 from 390 to 320 Ma; Figure 2) was coeval with renewed opening of the Canning Basin (the 373-Ma Pillara Extension; Romine et al., 1994) and the adjacent Bonaparte Basin (Mory & Beere, 1988; Figure 1a). Near the beginning of this period (approximately 370 Ma), the principal compressive stress directions in the ASO shifted from N-S to NNE-SSW. This change was due to displacement of the Euler rotational axes in the Gondwana and Laurussia supercontinents (Kröner et al., 2016). Metamorphism and deformation across the ASO are reduced for the period 360–340 Ma but spikes again with extensive sedimentation at approximately 340 Ma. After approximately 320 Ma, orogenic activity decreased in the ASO at the same time that the configuration of Gondwana and boundary stresses on the Australian plate significantly changed, possibly due to the shift of the paleo-longitudinal apparent northward wander path (i.e., continental drift) to the south of the Gondwana plate (Klootwijk, 2013).

### 2.3. Current Models for the Formation of the ASO

Discussion of the Paleozoic tectonics of the Australian continent is largely focused on the compressive N-S stresses responsible for intracontinental orogenesis, with authors rarely discussing the significance of westward paleo-Pacific subduction as one of the tectonic stress actuators for central Australia crustal deformation (e.g., Gray et al., 2004). This is primarily because an ~2,000-km distant westward subduction driver leading to a westward compressional momentum is at odds with the observed E-W structural architecture of the ASO (Figure 3a). Thus, the westward tectonic stress influences on central Australia orogenesis have largely been ignored. Studies by Roberts and Houseman (2001), Klootwijk (2013), and Kröner et al. (2016) correlate intraplate reactivation of central Australia with the mainly N-S convergence between Gondwana and Laurasia, forming the Qinling Orogen in the north (Figure 3a). Using numerical models, Roberts and Houseman (2001) showed that rotation of the north Australian block induced simultaneous extension of the Canning Basin in NW Australia and N-S convergence within an area of lithospheric weakness in central Australia. In this scenario, however, heterogeneous deformation within the ASO and the periods of compression and tectonic quiescence remain unexplained. Subsequently, Raimondo et al. (2014) focused attention on the episodic nature of the ASO, suggesting a causal link between ASO activity and periods of alternating E-W compression and extension related to subduction rollback affecting the Tasmanides. In both models, the zone of weakness in the center of the Australian plate is the Ordovician Larapinta seaway.

In the following simulations, we use numerical thin viscous sheet models to test (1) the effect of N-S compression on the deformation pattern within and around a single NW-SE trending weak zone, (2) the effect of the addition of an eastern weak wedge on that deformation pattern, and (3) the effect of compressional or extensional forces at the eastern boundary. With these models, we aim to reconcile the agreed and controversial features identified above (section 2). Our models build upon those performed by Roberts and Houseman (2001) by adding extra complexity, testing the hypothesis that the Tasmanides, as well as the weak crustal wedge comprising the HRG metasedimentary rocks, both played significant roles that influenced the timing and local kinematics of the ASO.

## 3. Numerical Implementations

### 3.1. Necessary Model Components

To simplify modeling of the large-scale effects associated with intracontinental orogeny at midcrustal to lower crustal levels, it is necessary to model behavior at the lithospheric scale with emphasis on the dominant ductile deformation active at shallower crustal depths. In addition, the following *ingredients* are necessary to perform the tests outlined above:

1. A regional-scale zone of weakness where strain is accommodated to form the intraplate orogen. This zone needs to be embedded in a relatively stiff continental plate that transmits plate boundary stresses. For the ASO, the proposed zone of weakness is the NW-SE oriented Larapinta seaway (Maidment, 2005) and its sedimentary infill, now largely incorporated into the ASO.
2. A localized zone of weakness that corresponds to the deep pre-ASO rift basin represented by the HRG (Maidment, 2005; Maidment et al., 2013; Tucker et al., 2015).

3. Plate boundary conditions that allow the effects of different boundary stresses to be tested. These should include the following:

(a) a fixed plate boundary to the south to represent the southern part of the Australian continent being stationary in a Gondwana-fixed reference frame;
(b) a northern boundary with N-S compressional stresses and a rotational component that simulates the effect of the Canning Basin opening coupled with N-S collisional forces in the north; and
(c) an eastern boundary that may be either tectonically passive, compressional, or extensional to model the Tasmanides' variable tectonic character through time.

### 3.2. General Numerical Model Setup: Rheological Flow Laws, Model Geometry, and Boundary Conditions

#### 3.2.1. General Model Used and Rheological Flow Laws

Here we use the nonlinear viscous finite element code BASIL (Barr & Houseman, 1996; Houseman et al., 2008), which allows monitoring of stress, strain, vorticity, and tectonic activity in the form of overthickening of the lithosphere. The continental lithosphere is represented by a thin viscous sheet layer, which deforms coherently. Deformation of the lithosphere is, in response to the deviatoric stress, determined by a nonlinear power law rheology (England & McKenzie, 1982):

$$\overline{\tau}_{ij} = B\dot{E}^{\left(\frac{1}{n}-1\right)}\dot{\varepsilon}_{ij} \tag{1}$$

where $\overline{\tau}_{ij}$ and $\dot{\varepsilon}_{ij}$ are the vertically averaged components of the deviatoric stress and strain rate tensors, respectively; $n$ is a constant referred to as the rheological exponent that determines the degree of nonlinearity; and $\dot{\varepsilon}$ is the second invariant of the deviatoric stress tensor. $B$ is a rheological constant that includes the dependence of the vertically averaged viscosity of the lithosphere (England & McKenzie, 1982). The distribution and value of the parameter $B$ (i.e., viscosity prefactor) can be spatially variable within the horizontal plane ($x$, $y$) to allow for investigation of the effect of a heterogeneous strength distribution in the lithosphere (i.e., values of 5 to 0.5). For the models presented in this contribution, $n = 3$ is used for the rheological exponent to represent the vertically averaged rheology of the lithosphere dominated by the power law creep of olivine (Karato et al., 1986).

The velocity distribution in the numerical model is used to determine the rate of crustal thickening in terms of the vertical strain rate at each ($x$, $y$) location:

$$\frac{1}{S}\frac{\partial S}{\partial t} = \left(\frac{\partial u}{\partial x} + \frac{\partial v}{\partial y}\right) \tag{2}$$

Equation (2) computes the crustal thickness distribution during lithospheric deformation. Erosion is not included, so crustal volume is conserved. The relative vorticity vector, perpendicular to the plane of calculation, is also obtained from the horizontal velocity field ($u$,$v$):

$$\zeta = \frac{\partial v}{\partial x} - \frac{\partial u}{\partial y} \tag{3}$$

#### 3.2.2. Model Geometry

The base geometry of the model has been chosen to be a thin viscous sheet with a ratio width ($X$)/length ($Y$) of 1:1.4, representative of the rough geometry of the Australian plate for this part of Gondwana at the time of ASO formation (Figure 3b). Distance in $X$ corresponds to separation between the western (Canning Basin) and eastern limits of the Larapinta seaway (~1,700 km); distance in $Y$ equals the N-S extent of the North and South Australian Cratons (~2,400 km). We assume a nominal lithospheric thickness representing $Z = 100$ km. Within the model, a preexisting zone of weakness is defined. It is represented by a lateral variation of the viscosity coefficient within a NW-SE band. In this zone of 450- to 600-km width, the viscosity is greater in the northern and southern parts of the lithospheric sheet but decreases perpendicular to the boundaries to a minimum in the middle of the weak region. In either side of the zone of weakness are located lithospheric blocks of uniform high viscosity. To test the influence of a wedge of extreme weakness to the east, a low-viscosity wedge-shaped block in the eastern extremity of the weak region is incorporated in some models (Figure 3b).

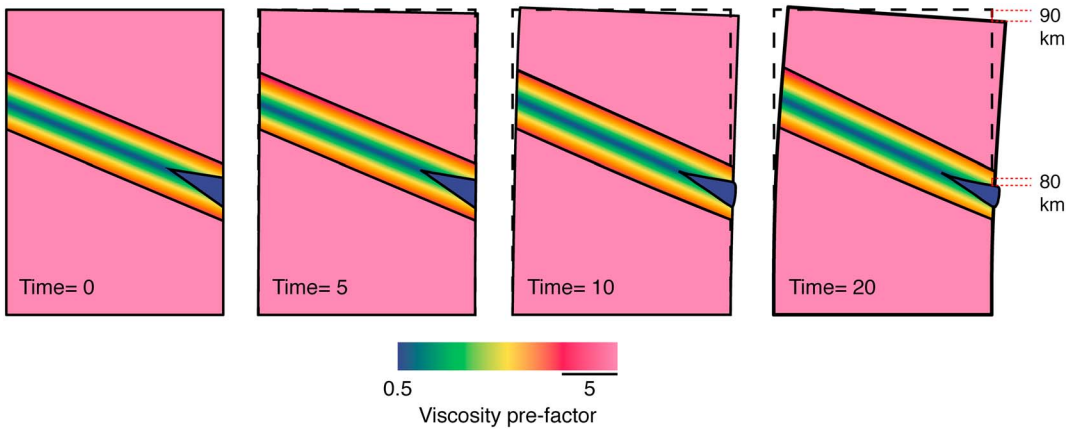


**Figure 4.** Example of the evolution of the model with (dimensionless) time; here, deformation of model M4b is presented for time 0, 5, 10, and 20. Displacement of the northern model boundary and northern weak wedge boundary in model units converted to kilometer are displayed.

One of the imposed features of the model is that boundaries to the zone(s) of weakness are oriented obliquely to the boundary tractions. Therefore, the model behavior will differ in the *x* and *y* direction. To capture this behavior, results are presented both as *XY* maps showing the spatial variations but also as transects oriented perpendicular to the structural grain, that is, perpendicular to the weak zone boundary (Figure 3b). Three transects are presented: Transect A cuts the center of the model; Transect B is the same length as Transect A, but displaced 0.77 model units (i.e., ~1,300 km) to the east; and Transect C is close to the eastern boundary of the model (0.6 model units in length). When compared to the ASO, Transects A–C roughly represent N-S profiles through the Reynolds-Anmatjira Ranges, Strangways Range, and Harts Range, respectively (Figures 1 and 3b).

#### 3.2.3. Boundary Conditions and Simulation Setup

The southern boundary ($y = 0$; tick-marked lower boundary in Figure 3b) is fixed with a velocity in *X* and *Y* set to 0 ($u = 0$, $v = 0$). The other boundaries (western: $x = 0$; eastern: $x = 1$; northern: $y = 1.4$; dashed external boundaries in Figure 3b) can all move in response to applied traction, positive or negative, normal or shear. For a model run, boundary forces are imposed on the model. To obtain the desired clockwise rotation of the northern block of the model, a south directed dimensionless stress is applied to the northern boundary (Figure 3b), varying linearly from $x = 0.5$ to $x = 1$, with a dimensionless magnitude of $\sigma_y = 0$ at $x = |0.0–0.5|$to $\sigma_y = -1$ at $x = 1.0$. In order to test the hypothesis that stresses applied to the eastern boundary ($x = 1$; Figure 3b) can influence the intraplate style and periodicity of deformation, two different approaches were used:

1. A lithostatic-stress boundary condition (Houseman & England, 1993) was imposed on all models for the western, eastern, and northern boundaries, where no positive or negative traction is imposed on the boundary. This lithostatic boundary condition assumes that the normal stress is constant and equal to the initial confining stress and presents zero tangential shear stress along the boundary. It allows the modeling of a weak external region and consequent free displacement of the boundary during the simulation; in the following, we call this condition *passive*.
2. On selected models, east-directed ($-\sigma_x$) or west-directed ($\sigma_x$) stresses were imposed on the total length of the eastern boundary (y = 0 to y = 1.4; Figure 3b). When active, the eastern boundary shows an applied dimensionless stress magnitude of 0.15, both for $\sigma_x$ and $-\sigma_x$.

All models are run using 20 dimensionless simulation time units (Figure 4). The running time of the experiment was selected in order to produce a specific amount of southern dislocation of the modeled northern boundary (corresponding in model units to ~100 km; Figure 4), for the model that best fits the observed geology of central Australia (Model M4b).

### 3.3. Models Tested

In our study, six models are used to perform our thin viscous sheet modeling. These have been chosen to test the causal relationships between (1) the velocity boundary conditions at the northern and eastern boundaries of the model, that is, whether the eastern boundary is passive or undergoing active compression or

**Table 1**
*Summary of Simulation Sets for the Numerical Model, Providing the Individual Parameters of Stress Activity and Added Block Geometry*

| Models | Weak zone band | Weak zone wedge | Principal stress regime | Secondary stress regime |
|---|---|---|---|---|
| M1 | X | | N-S compression | N/A |
| M2 | X | X | | N/A |
| M3a | X | | | E-W compression |
| M3b | X | | | E-W extension |
| M4a | X | X | | E-W compression |
| M4b | X | X | | E-W extension |

*Note*. N = north; S = south; E = east; W = west.

extension, and (2) the presence or absence of an extremely weak wedge at the eastern end of the weak band (Table 1 and Figure 5).

In all models, a south directed stress is applied to the northern boundary throughout the simulation, while the western boundary is *passive*. For Models M1 and M2, the eastern boundary is also passive. In contrast, for Models M3a/M4a and M3b/M4b, compressional (west directed) and extensional (east directed) tractions are applied along the eastern boundary, respectively (Table 1 and Figure 5).

All models have two blocks in the northern and southern regions with relatively high-viscosity prefactors of 5 (equation (1)) representing ~80% of the whole model. These blocks are separated by a weak band with the viscosity prefactor changing gradually perpendicular to the weak band edges, following a logarithmic sinusoidal function where the viscosity prefactor is 5 at the block-weak zone edge and 1 (equation (1)) in the center of the band. Models are presented with increasing complexity. The differentiator between models is the presence (Models M1, M3a, and M3b) or absence (Models M2, M4a, and M4b) of the extremely weak wedge with a viscosity prefactor of 0.5 (equation (1); Table 1 and Figure 5).

### 3.4. Model Results and Analysis

In thin viscous sheet calculations, there is an implicit assumption that the plane of the calculation is horizontal. Therefore, the relative vorticity is a measure of horizontal local spin, where it is defined that a positive or negative vorticity signifies crustal material flow rotating counterclockwise or clockwise, respectively.

The faulting style expected in a surficial brittle layer that coherently deforms with the viscous lithospheric sheet is quantified. The diagonalized strain rate tensor is decomposed at any point of the solution domain into a pair of double couples, following the method of Houseman and England (1986):

$$p = \left(\frac{3}{4} + \frac{1}{\pi}\ \tan^{-1}\left(\frac{\dot{\varepsilon}_2}{\dot{\varepsilon}_1}\right)\right) \tag{4}$$

The contour quantity between 0 and 1 indicates the expected type of deformation (i.e., style of near-surface faulting) as follows: thrust only ($0 < p < 0.25$), thrust + strike-slip ($0.25 < p < 0.5$), strike-slip only ($p = 0.50$), normal + strike-slip ($0.5 < p < 0.75$), or normal only ($0.75 < p < 1$). The $p$ quantity can thus exhibit the magnitudes of dip-slip and strike-slip deformation. In the range $0.375 < p < 0.625$, the strike-slip deformation rate exceeds the dip-slip deformation.

Model results for the total 20 simulations dimensionless time condition are shown as *XY* maps where only the area containing the weak band and wedge is visualized. In Figures 6 and 7, we present maps of (a) crustal vertical variation, (b) relative vorticity added with the velocity field, and (c) type of deformation (i.e., style of near-surface faulting).

## 4. The Effect of Boundary Conditions on Intracontinental Orogenesis: Results From Numerical Modeling

### 4.1. Simulation Sets

#### 4.1.1. Model M1: North Compression Only

Model M1 shows only minor displacement of the N, E, and W boundaries, all of them displaying a small rotational motion in map view (Figures 6 and S1 to S3). An incipient protrusion of material toward the east is visible on the eastern boundary close to the central sector of the weak band.

There is significant crustal thickening in the eastern convergent zone and crustal thinning in the western extensional zone, with an overall position and direction following the central E-W weak band from end to end (Figure 6a). All the transects show a crustal thickness distribution that is similar to a Gaussian profile, with minimum thickening at both edges of the transect, and a maximum thickness of 0.53, 0.55, and 0.56 localized in the central sector of the weak band for Transects A–C, respectively (Figure 8a).

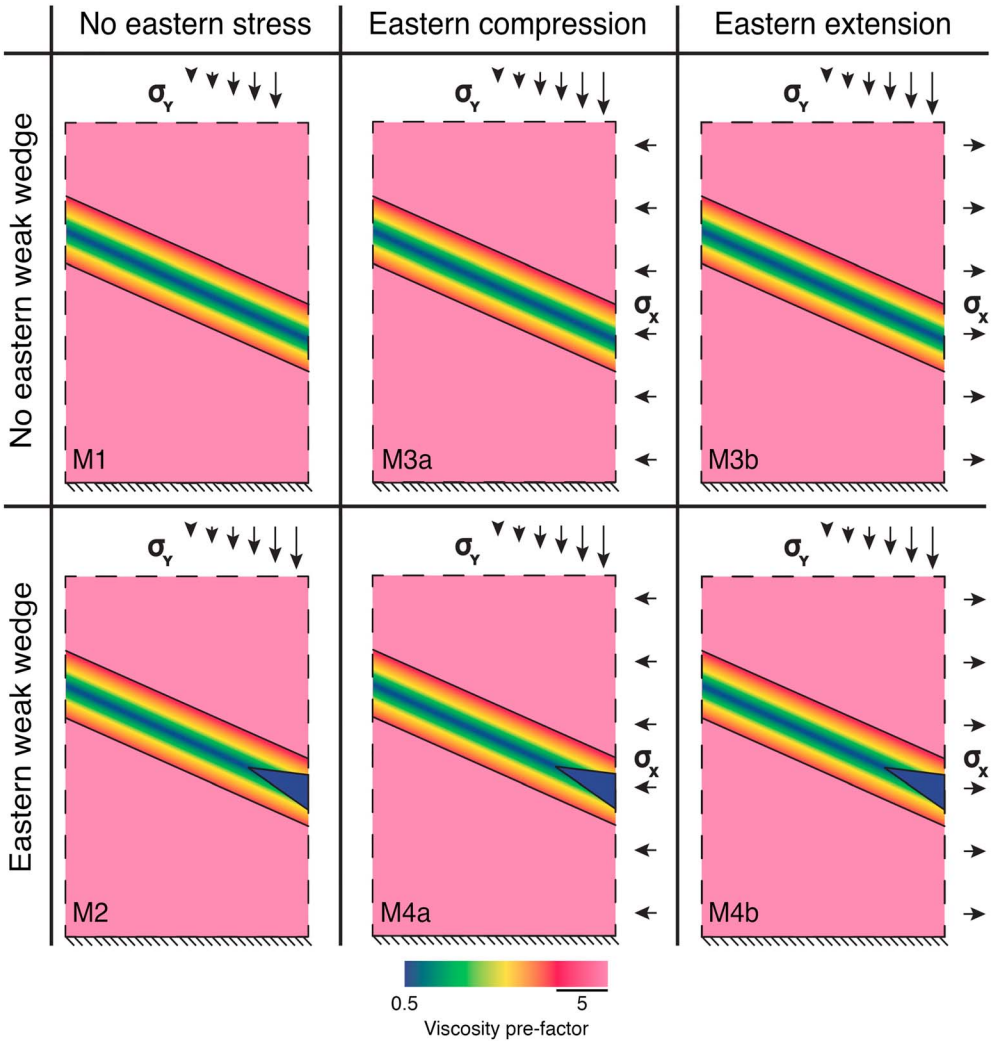


**Figure 5.** Geometry used in the numerical models. All models present active and equal value of south-directed principal stresses. The top row presents the models with no added weak wedge (M1, M3a, and M3b). The bottom row shows the models with the added weak wedge (M2, M4a, and M4b). The left column displays the models presenting no applied secondary eastern stress (M1 and M2). The middle column shows the models with the added secondary eastern stress-compressional (M3a and M4a). The right column presents the models with the added secondary eastern stress-extensional (M3b and M4b).

The vorticity distribution (Figure 6b) follows a similar pattern to crustal thickness, where the highest values of clockwise vorticity are seen in the center of the weak zone, with increasing values toward the eastern convergent sector. A small area near the eastern boundary, above the higher values and concentration of clockwise vorticity, shows a minor counterclockwise rotation. This pattern is confirmed by the vorticity transects (Figure 8b).

The distribution of the type of deformation (Figure 6c) shows a dichotomy of faulting between the W and E sector. The western sector exhibits primarily normal faulting, whereas the eastern sector presents thrust faults with strike-slip dominating in a transition zone. The northern half of the weak zone displays an area dominated by simple shear and a small amount of compression. Most of the weak band sector and southern area is dominated by thrust and subordinate shear, shifting to an enclaved area of thrust-only faulting in the center. Across the transects, from SW to NE, the faulting style changes from barely dominant shear faulting with subordinate thrusting, to a thrust-dominated area within the weak band for Transects B and C, to a thrust-only area in Transect A, inverting again for all transects toward a shear-dominated area in the northern part of the weak band (Figure 8c). A higher rate of change for the style of deformation is observed from a thrust-

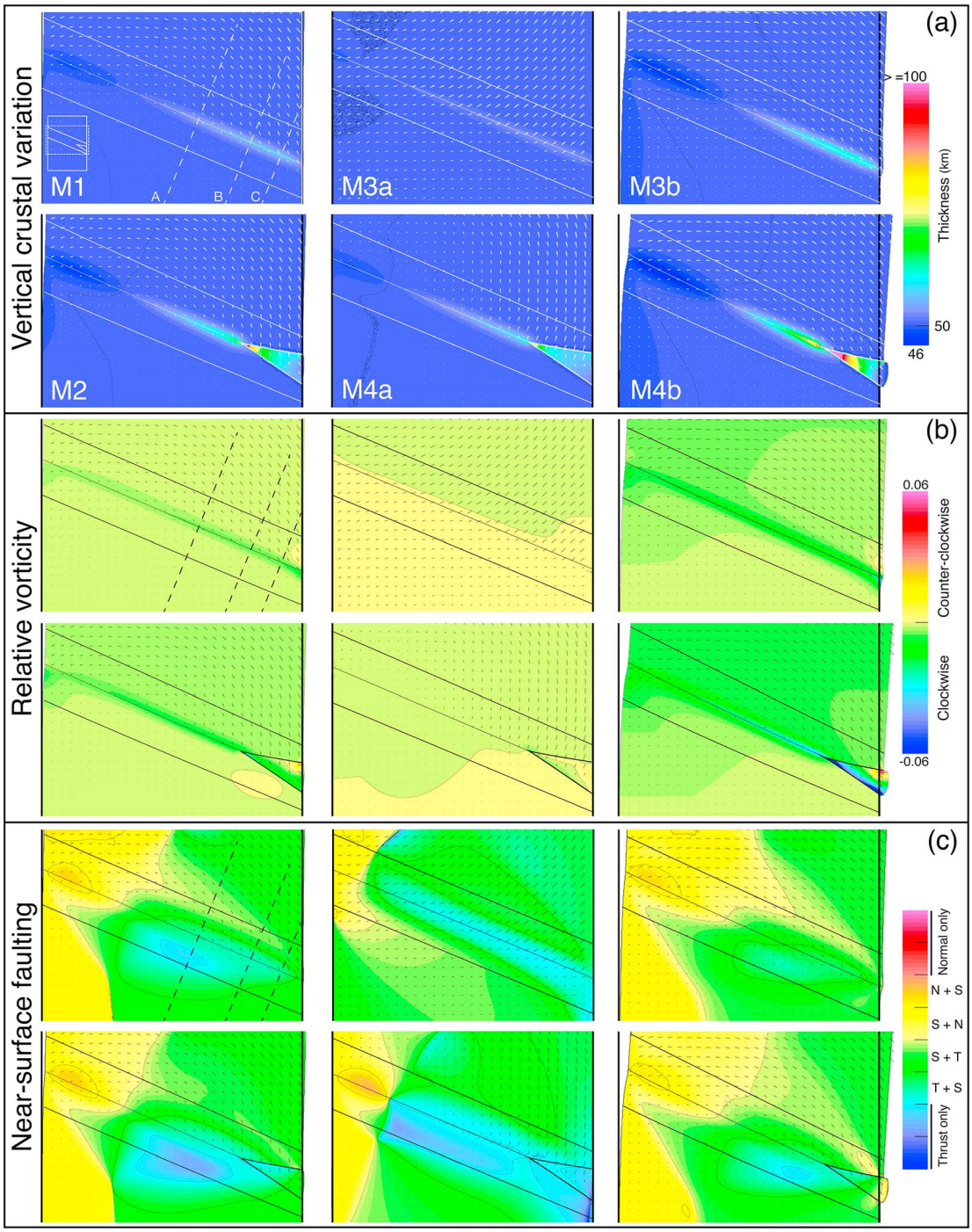


**Figure 6.** Snapshot at the final simulation dimensionless time 20 for (a) crustal vertical variation, (b) relative vorticity, and (c) near-surface faulting. The figures only display the area containing the weak band for each model, due to most of the relevant deformation observed being concentrated in this region. Transects A–C are displayed in Model M1.

dominated region (SW) for Transects B and C to a shear-dominated region (NE), compared to a similar style of deformation change observed for Transect A (in this case from a thrust-only region in the SW).

#### 4.1.2. Model M2: North Compression + Eastern Weak Wedge

Compared to Model M1, Model M2 exhibits a slightly higher displacement and rotational motion of the northern block, with a slightly enlarged protrusion along the eastern boundary (Figure 6 and S1 to S2).

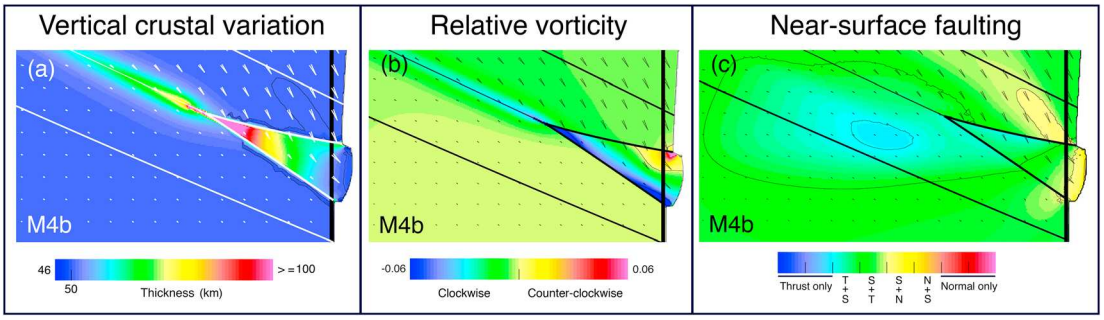


**Figure 7.** Enlarged region involving the eastern weak wedge for Model M4b, showing details of the features displayed in Figure 6.

Crustal thicknesses are higher compared to M1, especially in proximity to the pointed end of the wedge shape and within the eastern area of the weak wedge (Figure 6a). Inside the wedge, crustal thickness decreases from the western boundary to no thickening at the eastern boundary. Transect A (Figure 8a) shows a pattern of crustal variation almost identical to M1 except for the absolute thicknesses. In contrast, Transects B and C (Figure 8a) exhibit an abrupt increase in crustal thickness. For Transect B, comparing M1 (weak wedge

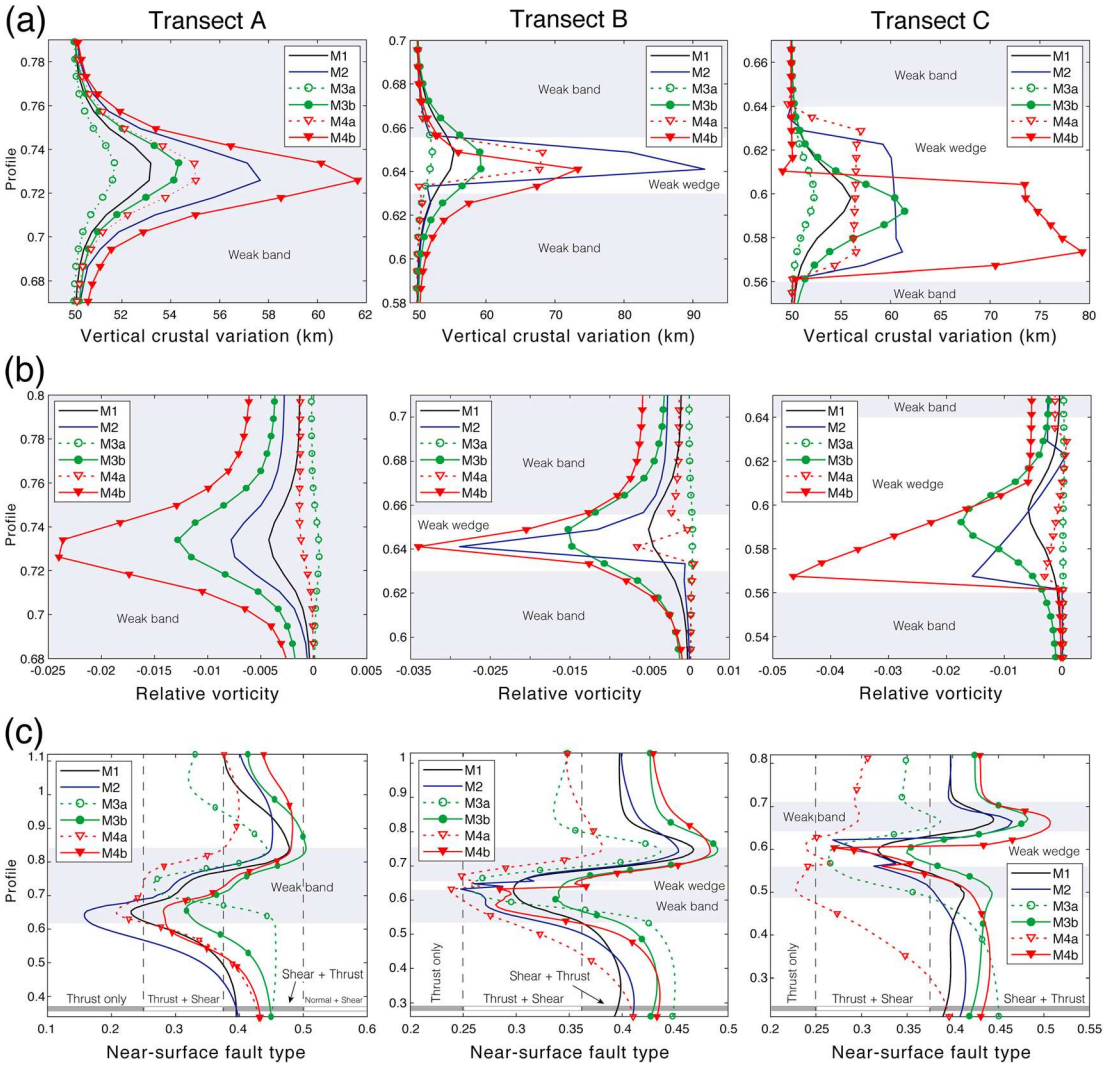


**Figure 8.** Variation in Transects A–C for the conditions of (a) vertical crustal variation, (b) relative vorticity, and (c) near-surface fault type for all models (M1 to M4b) after simulation dimensionless time 20.

absent) to M2 (weak wedge present), there is a significant contrast between the second lowest maximum crustal thickening for all simulations (M1) and the highest maximum crustal thickening for all simulations (M2) at approximately the same locale in the model.

A region of clockwise vorticity approximately follows the central region of the weak band (Figure 6b), the intensity of which is higher compared to M1, with the highest vorticity value close to the pointed end of the weak wedge. Within the wedge, two areas of distinct vorticity values are visible. To the south of the weak wedge, a circular area with diminished vorticity values is observable. Transect A follows the same pattern of vorticity seen in M1, only diverging with some higher absolute values (Figure 8b). Transect B shows abrupt increases in clockwise vorticity within the weak wedge, a change that is not observed in M1 without the wedge (Figure 8b). The same pattern observed for Transect B occurs for Transect C, however, instead of an abrupt increase of clockwise vorticity after crossing the northern boundary of the weak wedge, the vorticity builds in intensity toward its southern boundary, before decreasing almost instantaneously to 0 (Figure 8b).

The distribution and type of deformation are similar to M1, with the western sector showing normal faulting, whereas the eastern sector exhibits thrust-related faults (Figure 6c). Two areas show thrust-only faulting: one at the western edge of the weak wedge and a much smaller region external to the SW corner of the weak wedge, which is absent in M1 (Figure 6c). Involving these two areas and most of the weak wedge, a zone of thrust + shear exhibits increasing thrust dominance in the vicinity of the weak wedge boundaries. This thrust-dominant area is also located at the intersection between the two main orientation patterns observed in the model: E-W and NW-SE (Figure 6c). A region of normal faults only is present in the NW corner. Figure 8c reveals for all transects a higher overall amount of thrust-dominated faulting compared to M1. Similarly, all transects exhibit an equivalent distribution of fault types, starting from SW with a shear-dominated region, rapidly changing into a thrust-dominated region, followed by a thrust-only region (in Transects A and B only) near or within the weak band area. At the end of the transects, the faulting pattern returns to a thrust-dominated region. Transects B and C differ from Transect A by crosscutting the weak wedge, displaying an abrupt change from shear-dominated to thrust-dominated in the regions proximal to the boundaries of the weak wedge.

#### 4.1.3. Models M3a and M3b: North Compression + Active Eastern Boundary Stress (M3a—Compressive; M3b—Extensive)

Model M3a (compressional eastern boundary) exhibits comparatively no rotation or displacement of the free boundaries, whereas Model M3b (extensional eastern boundary) displays a high rotation and displacement of the northern block. No protrusion is observed for M3a, whereas M3b shows a slightly enlarged protrusion compared to M2 (Figures 6 and S1 to S3).

M3b exhibits localized crustal thickening in the eastern convergent zone and crustal thinning in the western extensional zone, reflecting M1 behavior, although with higher crustal thickening values in the east and a larger area of crustal thinning in the NW corner (Figure 6a). Dissimilar to M3b, M1, and M2, Model M3a presents a limited variation in crustal thickness that nevertheless follows the direction and position of M3b. Transects A–C mirror this crustal behavior, reaching maximum values in the center of the weak band (Figure 8a). Comparing all models, M3a displays lower overall values of vertical crustal variation.

M3b vorticity distribution is similar to that of Model M1, with higher overall values of clockwise vorticity located in the central zone of the weak band and in the eastern convergent sector (Figure 6b). However, absolute vorticity values for M3b are increased relative to M1. The velocity field exhibits a more south directed motion of the crustal flow regime close to the eastern boundary, and by association, is more perpendicular to the weak band (Figure 6b). In M3b, the flow velocity within the weak band also presents higher values compared to M1. To the east of this location, two patches of clockwise and counterclockwise vorticity are discernible. Contrary to M3b, Model M3a shows almost no vorticity for the entire model area (Figure 6b). For Model M3b, Transects A–C exhibit a similarly smooth Gaussian behavior for vertical crustal variation as M1 (Figure 8b). In contrast, Model M3a displays an almost completely flat behavior and close to null values for vorticity (Figure 8b).

M3b exhibits a pattern of deformation similar to that presented by M1. For both models, normal faulting dominates in the west and thrust faulting dominates in the east, with similar localization and relative shape of these isolated regions. However, M3b displays a more intensely sheared model than M1 (Figure 6c). Figure 6c shows that the areas dominated by the coaxial component of deformation in previous models display higher shear stress components in M3b. Model M3b also shows greater invasion of the western normal-dominated faults into the eastern area compared to all previous models. Contrary to M1 and M3b, Model M3a

exhibits an almost entirely thrust-related type of deformation, with normal faulting confined to the NW area of the model (Figure 6c). The thrust-dominated area for M3a is mostly localized within the weak band, presenting a more equilibrated thrust/shear ratio in the NE region of the model. All remaining areas of M3a present shear + thrust faulting, with an increased shear component in the southern area of the model (Figure 6c). For both M3a and M3b, Transects A–C exhibit a gradual variation in the rate of deformation along the length of each transect, when crossing boundaries that mark the change from thrust-dominated to shear-dominated faulting and vice-versa (Figure 8c).

#### 4.1.4. Models M4a and M4b: North Compression + Active Eastern Boundary Stress (M4a—Compressive; M4b—Extensive) + Eastern Weak Wedge

Similar to M3a, Model M4a shows no rotation or displacement of the free boundaries, whereas Model M4b displays a high rotation and displacement of the northern block. For M4b, the protrusion at the eastern boundary exhibits a significantly increased displacement of crustal material, whereas M4a exhibits a lack of extrusion similar to that seen in M3a (Figures 6, 7, and S1 to S3).

Despite M4b exhibiting the highest crustal thicknesses, the general pattern of crustal variation is similar to that seen in M2. In contrast, M4a exhibits overall lower crustal variations. For both M4a and M4b, Transects A–C show a progressive increase in crustal thickening (Figure 6a). Similar to M2, Transect A displays a smooth distribution of crustal thickening, whereas Transects B and C present high increases or decreases in crustal thickening when crossing the boundary of the weak wedge.

M4b exhibits a similar vorticity pattern to M2 but only outside of the weak band (Figures 6b and 7b). Compared to the other models, M4b shows values that are substantially higher for both vertical crustal variation and vorticity. This increase in magnitude is well observed between M4b and M4a, wherein the latter, the spatial pattern of vertical crustal variation and vorticity is similar to M4b, but with significantly lower values. Exclusive to M4b, an apparent stratification of the vorticity intensity inside the eastern weak wedge is discernible, where a gradually shifting pattern of strongly clockwise in the SW to counterclockwise in the NE is seen (Figures 6b and 7b). Within the weak wedge of M4b and opposite to M4a, the velocity vectors show the material flow deflecting from NW-SE to approximately ESE, with higher magnitude close to the northern boundary (Figure 7b). Model M4a displays very small values of vorticity for the entire model, increasing slightly in the southern region of the weak wedge (Figure 6b). For M4b, Transects A–C follow the same vorticity path as M2, only diverging at the highest values (Figure 8b). Transect A exhibits a smooth distribution of vorticity in the weak band, whereas Transects B and C present abrupt vorticity variations at the boundaries of the weak wedge and a gradual increase from N to S within the wedge. All transects of Models M4a and M3a present a similar vorticity distribution for low-vorticity values (Figure 8b). The differentiation between these two models resides in the higher vorticity values situated close to the southern boundary of the weak wedge for M4a. These higher values are reflected by a slight increase in vorticity, followed by an abrupt decrease passing the boundary of the weak wedge (Figure 8b).

M4b presents a similar fault distribution to M2 (Figures 6c and 8c) but with a more shear-dominated type of faulting. Two areas of normal faulting are visible close to the eastern boundary: one above the weak wedge with a NW-SE longitudinal direction and the other at the eastern margin of the protrusion from the weak wedge (Figure 8c). The thrust-dominated area is located in the western sector of the weak wedge and its western margin. Within this area, some regions show a higher proportion of thrust versus shear fault displacement, located to the south of the northern and southern boundaries of the weak wedge and to the west of the weak wedge. In contrast, M4a is characterized by thrust-dominated faulting for the most part (Figure 6c). Thrust-only areas are situated within the weak band and across almost the totality of the weak wedge area. Transect A shows a similar pattern of faulting for both M4a and M4b, specifically in terms of abrupt changes in direction along the *x* axis (Figure 8c). However, M4a displays a more thrust fault-dominated distribution than M4b, visible as a shift from the center of the weak band in M4a to a region at the south of the weak band in M4b (Figure 6c). Transect B presents a similar pattern to Transect A but with a more extensive and abrupt change in the type of deformation, especially for M4b close to the northern boundary of the weak wedge (Figure 8c). For Transect C, M4b shows the same pattern visible in Transect B of extensive and abrupt changes in fault type when crossing the region close to the weak wedge (Figure 8c). Nevertheless, Transect C exhibits a larger contrast of faulting type between the interior of the weak wedge and the northern area. For Model M4a, Transect C shows a more gradual change in the type of deformation, and an extensive change in fault variability is absent for the top half of the transect.

### 4.2. Effect of Primary Versus Conjugated Primary and Secondary Stress Regime on Deformation Style, Crustal Thickening, and Eastern Extrusion

Our simulations show that the pattern of deformation in terms of crustal thickening, vorticity, and fault-type changes significantly when a secondary boundary stress is applied with a vector at a low angle to the structural grain of the weak zone. For all models, the localization of crustal displacement and deformation in the model is almost exclusively confined to the northern sector (Figures 6 and S1 to S3). The pattern of the velocity field, with the exception of Model M3a, shows that the lithospheric flow of material follows a clockwise rotation with northeast direction and relatively lower magnitude in the NW sector of the models, to a SSE direction and high magnitude along almost all of the eastern boundary (Figures 6 and S1 to S3). This motion is in accordance with Roberts and Houseman (2001), who found that clockwise rotation of the northern block relative to the southern block can activate the simultaneous opening of the Canning Basin to the west and compressional orogenesis in the Arunta Region to the east.

In a general sense, the models that present conjugated south directed compression and east directed traction (M3b and M4b; Figures 6 and S1 to S3), exhibit a higher amount of displacement of the model edges toward east and south relative to the models that present only a primary north stress regime (M1 and M2). Using 90 km of south directed displacement of the northern boundary (Figure 4) and with time constrained by the duration of ASO metamorphic activity (~80 Ma; Figure 2), the localized maximum N-S shortening rate at the northern boundary is 1.125 mm/year (or km/Ma) for the model showing the highest overall deformation (M4b). Due to a shorter southern displacement of 80 km at the northern boundary of the weak wedge (Figure 4), the strain rate is reduced to 1 mm/year (or km/Ma) for this area.

The enhanced rotation of the northern block presenting conjugated north and east directed compressive stress regimes allows for a higher amount of crustal thickening in the eastern sector, while also permitting a global increase in vorticity and shearing within the model (Figures 6 and 8). In contrast, models that present conjugated north compressive and west directed extensional stress regimes (M3a and M4a) have edges that are almost stationary or in some cases slightly moved toward the west for parts of the eastern boundary (Figures 6 and S1 to S3). The lack of motion of the northern block in M3a and M4a reflects the competing nature of compressive orthogonal stress regarding the deformation of the model. In these models, all patterns are inverted relative to M3b and M4b, with decreased thickening, vorticity, and a shift from shear-dominated to thrust-dominated faulting (Figures 6 and 8). Furthermore, if secondary stresses are present, a clear difference in thickness variation, vorticity asymmetry, and type of deformation is observed compared to the models where secondary stresses are absent (Figures 6 and 8).

Taking, for example, Models M4a and M4b, if extension as a secondary stress was followed by compression, we would expect rotation of the northern block to be accompanied by a large amount of crustal protrusion within the weak wedge, and a high amount of thickening, asymmetry in vorticity, and thrust-dominated and shear-subordinate type of deformation (Figures 6 and 8). The compressional period that follows would possibly displace the northern block westward and deactivate the crustal flow to the east in the wedge protrusion. It is possible that the protrusion will act as a stress buffer, allowing some N-S stress accommodation within the weak wedge. This stress accommodation would allow for a small amount of the deformation pattern observed in M4b (Figures 6 and 8).

### 4.3. Effect of Weak Zone Geometry on Model Behavior

The deformational behavior of our simulations is strongly affected by the presence or absence of the eastern weak wedge (Figures 6 and 8). The pattern of the velocity vector shows that for all models except M3a and M4a, the lithospheric material flow follows a clockwise rotation with NE direction and relatively low magnitude in the NW sector to a SE direction and high magnitude along almost all of the eastern boundary (Figures 6 and 8). Material flows almost perpendicular to the northern boundary of the weak wedge and is then deflected to an approximate ESE direction inside the wedge (Figures 6 and 7) in accordance with the lateral extrusion.

The presence of an eastern weak wedge (Models M2, M4a, and M4b; Figures 6a and 8a) results in higher crustal thicknesses, especially in the western sector of the wedge-shaped zone (Figures 6a and 7a). In contrast, models without the weak wedge show an overall lower and more homogeneous crustal thickness in the eastern sector, with its position and orientation following the central gradual low viscosity band (Figure 6a).

**Table 2**
*Summary Table Presenting for Each Individual Model a Semiquantitative Interpretation of the Observed Model Deformation*

| Models | | Northern block rotation | Protrusion from wedge in east | Crustal thickening | Asymmetry in vorticity | Dominant near-surface fault type |
|---|---|---|---|---|---|---|
| Without wedge | M1 | * | * | * | * | T + S > S + T |
| | M3a | - | - | Residual | Residual | T + S |
| | M3b | *** | ** | ** | ** | T + S; S + T |
| With wedge | M2 | ** | * | **** | *** | T + S > T only |
| | M4a | - | - | *** | Residual | T only > T + S |
| | M4b | ***** | ***** | ***** | ***** | T + S > S + T |

* = representation of quantity or intensity; T = thrust; S = shear.

The velocity vector representing the local direction of crustal flow and magnitude shows that all models except M3a and M4a present a central clockwise vorticity band that approximately follows the gradual low-viscosity band (Figure 6b). An apparent stratification of the vorticity intensity is visible inside the eastern weak wedge (Figures 6b and 7b). This vorticity stratification follows a gradual shifting pattern of highly clockwise in the SW to counterclockwise in the NE. Models M3a and M4a present no significant vorticity values or any highly localized vorticity sectors (Figure 6b).

Based on the distribution of deformation types, models that include the eastern weak wedge show an increased heterogeneity of fault patterns for the eastern central sector (Figure 6c). In M2 and M4b, a relative increase in thrust faulting is seen compared with the wedge-absent models, specifically close to the north and south boundaries of the weak wedge (Figures 6c and 7c).

## 5. Discussion

### 5.1. Localization of Intracontinental Deformation: General Model Behavior and First-Order Comparison With the ASO

The deformation pattern of the ASO (Ballèvre et al., 2000; Cartwright et al., 1999; Collins & Teyssier, 1989; Hand & Sandiford, 1999; Mawby et al., 1999; Raimondo et al., 2011, 2014; Figure 1) is generally well represented in our simulations. In particular, Model M4b best represents the deformation history (Table 2). Overall, the localization of thickening at the lithospheric scale is concentrated within weak parts of the crust at a low angle to the principal stress (Figures 6a–8a and 9). This localized deformation is in accordance with two of the requirements to form intracontinental orogens: (1) the transmission of far-field stresses from relatively strong plate margins (Handy & Brun, 2004; Shaw et al., 1991) and (2) a rheologically weak plate interior to accommodate the transmitted stress (Cunningham, 2013; Raimondo et al., 2011, 2012; Sandiford & Hand, 1998; Walter et al., 1995). Stress accommodation in weaker areas translates into lithospheric-scale thickening, more prominent in models with active extension along the eastern margin, and in areas where N-S compression is facilitated by structural and rheological controls (Figures 5–9 and Table 2). This is accompanied by changes in the type of faults in areas of contrasting crustal rheology, which act as mechanical weaknesses to localize strain (Maidment, 2005; Molnar & Dayem, 2010; Raimondo et al., 2011, 2012). The pattern of vorticity within the weaker areas matches the different types of crustal flow within the models (Figures 5–8 and Table 2). The orientation of preexisting crustal structures in the SE Arunta Region also plays a role in the strain-inducing accommodation of compressive stress (Hurd & Zoback, 2012; Thomas & Powell, 2017). This can be observed in models where crustal deformation is generally oriented at low angle to the principal stress component (Figures 5–9).

### 5.2. The Evolution of the ASO With Respect to Stress Evolution and the Presence of Localized Weak Zones

#### 5.2.1. Episodic Nature of ASO: Causes and Effects

The ASO comprises a series of episodic deformation events spanning the period 450–300 Ma, which reactivated an extensive and anastomosing mesh of Proterozoic shear zones and exhumed lower crustal rocks in the Arunta Region (Ballèvre et al., 2000; Cartwright et al., 1999; Collins & Teyssier, 1989; Hand & Sandiford, 1999; Mawby et al., 1999; Raimondo et al., 2011, 2014; Figures 1 and 2). The ASO exhibits large variations in metamorphic activity and basin evolution over its 150-Myr window of activity. There is a broad

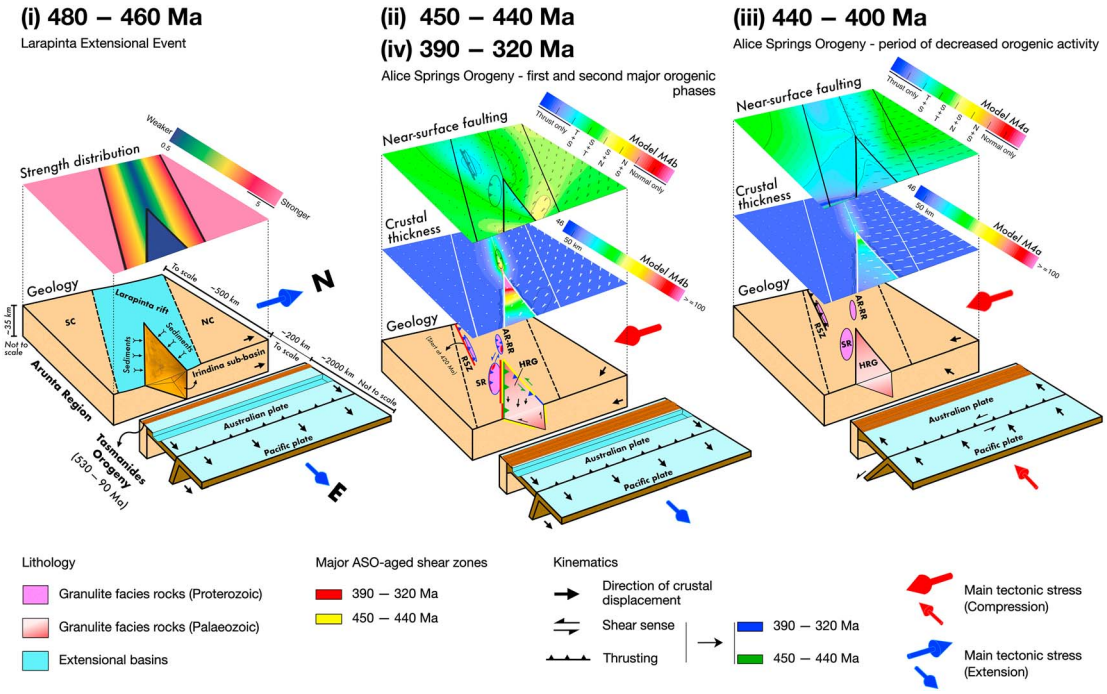


**Figure 9.** Schematic block models representing the geology of the Arunta Region of central Australia and the Tasmanides Orogeny at the start of the ASO (end of period (i)) and during distinct compressional and/or extensional stress regimes (ii, iii, and iv) at the northern and eastern Australian plate boundaries. The numerical model (M4a or M4b; Figures 6 and 7) best representing the fault and crustal thickening patterns observed on each orogenic phase of the ASO (ii, iii, and iv) is overlain on top of the Arunta Region schematic geology and tectonic setting for each of the previously mentioned time periods. Abbreviations: AR, Anmatjira Range; HRG, Harts Range Group; NC, North Australian Craton; RR, Reynolds Range; RSZ, Redbank Shear Zone; SC, South Australian Craton; SR, Strangways Range.

correlation between periods of retreating or stagnant westward subduction of the Pacific plate and an increase in metamorphic activity and synorogenic sedimentation across the ASO (Figure 2). In contrast, westward or northwest advancement of the Pacific plate is broadly correlated with a decline in both the metamorphic and sedimentary record of the ASO. This pattern of positive feedback between a retreating or stagnant Pacific plate and deformation in the ASO is observed in the models presenting inactive eastern boundary stresses (M1 and M2) or tractional, extensional eastern boundary stresses (M3b and M4b; Figures 6a–8a and 9). These models show that enhanced mountain building (high crustal thicknesses) and rotation of the northern block occurs when the eastern boundary is passive or actively extending (Roberts & Houseman, 2001; Figure 9). The negative feedback of an advancing Pacific plate on intraplate orogenesis is also visible in the models presenting eastern compressional stresses (M3a and M4a; Figures 6–9), which exhibit lower overall crustal thicknesses and limited northern block rotation due to the constrained displacement and rotation of the northern boundary (Table 2 and Figures S1 to S3).

### 5.2.2. Metamorphic Grade and Exhumation Patterns

The increase in metamorphic grade and pervasiveness of fluid hydration/retrogression in the Arunta Region from the northwest (Reynolds-Anmatjira Ranges) to the southeast (Harts Range) (Mawby et al., 1999; Raimondo et al., 2011, 2014; Tucker et al., 2015) can be explained by an increase in positive vertical crustal variation along the same trajectory observed in models with the eastern weak wedge present. In Models M2, M4a, and M4b (Figures 6a–8a, 9 and Table 2), higher crustal thickening is present toward and inside the eastern weak wedge, corresponding to the highest metamorphic grades of the HRG. This general pattern and the magnitude of crustal exhumation are observed in the vertical crustal variation maps shown in Figure 6. For Transect B (Figure 8a), Models M4a and M4b show crustal thickening values in the order of ~20–25 km. This is likely due to the bivergent shape of the Irindina subbasin and is similar to the observed patterns of exhumation along the western margin of the Harts Range (Maidment, 2005; Tucker et al., 2015).

The localization of higher crustal thickening is not randomly distributed in the Arunta Region (Figure 1b). As proposed by a number of authors (e.g., Cunningham, 2013; Klootwijk, 2013; Molnar & Dayem, 2010; Raimondo et al., 2014; Roberts & Houseman, 2001; Sandiford & Hand, 1998; Shaw et al., 1991), crustal thickening in intracontinental orogens is usually preferentially located in regions of weakened rheology, leading to enhanced strain accumulation in structures at a low angle relative to the principal stress component and in regions adjacent to crustal strength heterogeneities. In our case, the central sector of the low-viscosity band and the eastern weak wedge (Figures 6–9) model such localization. These two regions correspond to the SE Arunta Region and the western sector of the Harts Range due to their orientation and weakened rheology, respectively (Figure 1b). The opening of the Canning Basin is another example of deformation driven by weakened rheology, as previously discussed by Roberts and Houseman (2001). This feature can be observed in our models as crustal thinning within the western sector of the low-viscosity band, coeval with ASO activity (Figure 6).

Exhumation of granulite facies lower crust is not observed for the whole of the Arunta Region, instead of being concentrated in two major areas (Figure 1b). The kinematics of deformation in Models M2 and M4b (Figures 6c–8c; eastern weak wedge and neutral or extensional Tasmanides) shows two principal areas of thrust-dominated faulting, one proximal to the south of the weak wedge, with thrust predominance near the boundaries of the wedge, and the second to the southwest of the wedge. In the Arunta Region, these features can be spatially related with the development of two major thrust systems that expose lower crustal granulites in their hanging walls: (1) the Redbank Shear Zone, which involves ~25-km displacement of a mantle wedge to shallower crustal levels (e.g., Goleby et al., 1989, 1990; Korsch et al., 1998), and (2) the Harry Creek Shear Zone, which marks the southern margin of the Strangways Range basement terrane (Figures 1b and 9). These results suggest that the variations in metamorphic grade across the ASO are a consequence of differential exhumation. In other words, the general west to east increase in metamorphic grade is not a postorogenic feature caused by tilted exposure but rather represents a primary orogenic feature that implies what is observed in the east is not necessarily predicted to lie beneath the western Arunta Region.

The northern sector of the Harts Range records sinistral shear deformation in the Delny and Entire Point Shear Zone (Collins & Teyssier, 1989; Weisheit et al., 2016). Model M4b, and to a lesser extent Model M2 (Figures 6b–8b), shows higher values for vorticity in the Harts Range area compared with all remaining models (Table 2). These vorticity values can be explained by the west directed protrusion and flow of crustal material inside the weak wedge (Figures 6b and 7b), similar to the channel flow extrusion documented in the Himalaya-Tibetan Plateau (Beaumont et al., 2001; Bird, 1991; Godin et al., 2006) and hypothesized by Klootwijk (2013) for the intraplate Australian continent. This movement of material inside the wedge would imply both sinistral and dextral strike-slip kinematics along the northern and southern boundaries of the wedge, respectively (Figure 6b–8b and 9). However, the southern boundary of the Harts Range does not present any major dextral shear sense (Collins & Teyssier, 1989). This can be explained by either the distance of the laminar flow of crustal material (low vorticity) from the southern boundary or the low velocity of the flow (Figure 8b). The shape of HRG buried beneath the Mesozoic-Cenozoic sediments to the east (Figure 1b; Maidment, 2005) is consistent with the flow velocity of the extrusion having been higher in the northern part of the extrusion than in the south. This N-S dichotomy in the material flow velocity within the weak wedge potentially played an important role in the formation of a pull-apart region in the lower crust of the HRG, essential for the formation of the Entia Gneiss Complex double dome (e.g., Rey et al., 2017; Whitney et al., 2004) during the compressive ASO. Model M4b is the only model that shows a similar N-S dichotomy in the extrusion flow velocity (Figures 6b–8b), indicating that the presence of the eastern weak wedge conjugated with eastern extensional boundary forces is necessary to achieve this flow pattern.

#### 5.2.3. Fault Zone Types and Their Distribution: Reactivation and Changing Character

The Arunta Region shows widespread reactivation of Proterozoic shear zones throughout most of its SE domain during the ASO (Ballèvre et al., 2000; Cartwright et al., 1999; Raimondo et al., 2011, 2014). Reactivation is enhanced in areas proximal to the HRG (e.g., West Bore, Gough Dam, Entire Point, and Delny Shear Zones) and the Redbank Shear Zone (Figure 1). Adjacent to the West Bore and Gough Dam Shear Zone, and in a lesser amount between the Entire Point and Delny Shear Zones, a network of kilometer-scale hydrous shear zones is observed. The presence of hydrous shear zones bounding the HRG can be explained by local weaknesses and strain localization at the transition between the Paleozoic HRG

and Paleoproterozoic granulites of the Strangways Range (West Bore and Gough Dam Shear Zones), due to rheological heterogeneities between these two terranes (Molnar & Dayem, 2010; Figure 1c).

Such local weaknesses are observed in Transects B and C, with abrupt changes in crustal variation, local vorticity, and shifting of fault kinematics to thrust-dominated deformation at the boundaries of the eastern weak wedge (Figure 8). Since a local area of weakness governs the observed differences in movement, a large-scale Rayleigh-Taylor instability is incompatible because it is not predicted to cause localized changes in viscosity/rheology (Neil & Houseman, 1999; Raimondo et al., 2014). Compared with models including the eastern weak wedge, those excluding the weak wedge (M1, M3a, and M3b; Figure 6) do not show the same heterogeneity of crustal variation, vorticity, or kinematics of deformation. Instead, the strain deformation follows a smoother pattern due to the rheological control on the gradual change of viscosity in the weak band (Figure 6c). The lack of spatial heterogeneity for all calculated crustal parameters does not agree with the complex kinematic pattern and structural control observed in central Australia (Figure 1).

The orientation of preexisting Proterozoic structures also influences the timing of reactivation and the large-scale orogenic architecture. During the first major period of metamorphic activity (D1; Figure 2), the principal stress component is oriented N-S (Kröner et al., 2016), leading to the reactivation of structures oriented E-W, orthogonal to the first-order compressional stress (e.g., the Redbank Shear Zone; Biermeier et al., 2003). In our simulations, this area is approximately located in the domain representing the SW Arunta Region, where the thrust regime is dominant (Figures 6c, 7c and 9). This thrust-dominant area is also located at the intersection between the two main orientation patterns observed in the models: E-W and NW-SE (Figures 6c, 7c and 9). These two orientations match the dominant structural fabric of shear zones and thrust faults throughout the Arunta Region (Figure 1). During the second major period of metamorphic activity (D2; Figure 2), the principal stress was oriented NNE-SSW (Kröner et al., 2016), reactivating most of the shear zones and thrust faults oriented NW-SE to WNW-ESE (e.g., anastomosing shear zones in the Reynolds-Anmatjira Ranges and Strangways Range; Ballèvre et al., 2000; Cartwright et al., 1999; Raimondo et al., 2011, 2014). In our model, these structures are in a similar orientation to the main weak zones (i.e., the weak band and weak wedge), representing the Larapinta Rift and the Harts Range, respectively (Figures 6c and 9).

## 6. Conclusion: How to Make an Intracontinental Orogen: Relationships and Predictions

Here we demonstrate that in order to obtain a pattern of deformation similar to that observed for the Alice Springs Orogen, central Australia, external tectonic stresses acting on the margins of the Australian plate are required to be transmitted into areas of weak intraplate lithosphere. Secondary stresses orthogonal to the principal stresses may have positive or negative feedback on crustal thickness and rotation in the developing intracontinental orogen, by either enhancing or neutralizing the horizontal stress state acting on the weak areas. For the case study presented, our models show that the secondary stresses acting on the Australian continent contributed to marked periodicity during the ASO, as indicated by a strong temporal link between tectonic activity in eastern and central Australia.

Intracontinental orogenesis is sensitive to stress reconfigurations at plate margins. Primary features such as the geometry of the orogenic system, preexisting crustal structures, and transmitted stresses are highly relevant in the accommodation and concentration of differential stress within continental plates. When the principal transmitted stresses are oriented at a low angle to the weak intraplate zone, intracontinental orogenesis is enhanced. A higher magnitude of crustal thickening rates in the context of these models implies exhumation of higher grade metamorphic rocks, augmented by enhanced thrusting when coupled with proximal boundaries of contrasting rheological terranes or the presence of previous crustal weaknesses (e.g., shear zones or a failed rift). Secondary stresses may also provide a positive effect for the principal stresses and enhance the extrusion of lower crustal material from the weak areas.

**Acknowledgments**
This is contribution 1209 of the Australian Research Council (ARC) Centre of Excellence for Core to Crust Fluid Systems. This work was carried out as part of a PhD study at Macquarie University and was supported by ARC Discovery grant DP160103449. We thank Russ Pysklywec and an anonymous reviewer for constructive reviews and Taylor Schildgen for editorial handling. We are grateful to Robin Gardner for invaluable help in using Basil software and for useful modelation discussions. The data used are listed in the references, figures, tables, and supporting information.

## References

Aitken, A. R. A., Betts, P. G., & Ailleres, L. (2009). The architecture, kinematics, and lithospheric processes of a compressional intraplate orogen occurring under Gondwana assembly: The Petermann orogeny, central Australia. *Lithosphere*, *1*(6), 343–357. https://doi.org/10.1130/L39.1

Andeweg, B., De Vicente, G., Cloetingh, S., Giner, J., & Muñoz Martin, A. (1999). Local stress fields and intraplate deformation of Iberia: Variations in spatial and temporal interplay of regional stress sources. *Tectonophysics*, *305*(1–3), 153–164. https://doi.org/10.1016/S0040-1951(99)00004-9

Ballèvre, M., Möller, A., & Hensen, B. J. (2000). Exhumation of the lower crust during crustal shortening: An Alice Springs (380 Ma) age for a prograde amphibolite facies shear zone in the Strangways Metamorphic Complex (central Australia). *Journal of Metamorphic Geology*, *18*(6), 737–747. https://doi.org/10.1046/j.1525-1314.2000.00289.x

Barr, T. D., & Houseman, G. A. (1996). Deformation fields around a fault embedded in a non-linear ductile medium. *Geophysical Journal International*, *125*(2), 473–490. https://doi.org/10.1111/j.1365-246X.1996.tb00012.x

Beaumont, C., Jamieson, R. A., Nguyen, M. H., & Lee, B. (2001). Himalayan tectonics explained by extrusion of a low-viscosity crustal channel coupled to focused surface denudation. *Nature*, *414*(6865), 738–742. https://doi.org/10.1038/414738a

Bendall, B. (2000). Mid-Palaeozoic shear zones in the Strangways Range: A record of intracratonic tectonism in the Arunta Inlier, Central Australia (Unpublished doctoral dissertation). Adelaide, Australia: University of Adelaide.

Biermeier, C., Stüwe, K., Foster, D. A., & Finger, F. (2003). Thermal evolution of the Redbank thrust system, central Australia: Geochronological and phase–equilibrium constraints. *Tectonics*, *22*(1), 1002. https://doi.org/10.1029/2001TC901033

Bird, P. (1991). Lateral extrusion of lower crust from under high topography in the isostatic limit. *Journal of Geophysical Research*, *96*(B6), 10,275–10,286. https://doi.org/10.1029/91JB00370

Braun, J., & Shaw, R. (1998). Contrasting styles of lithospheric deformation along the northern margin of the Amadeus basin, central Australia. *Structure and Evolution of the Australian Continent*, 139–156. https://doi.org/10.1029/GD026p0139

Braun, J., & Shaw, R. (2001). A thin–plate model of Palaeozoic deformation of the Australian lithosphere: Implications for understanding the dynamics of intracratonic deformation. *Geological Society, London, Special Publications*, *184*(1), 165–193. https://doi.org/10.1144/GSL.SP.2001.184.01.09

Buick, I., Miller, J., Williams, I., & Cartwright, I. (2001). Ordovician high-grade metamorphism of a newly recognised late Neoproterozoic terrane in the northern Harts Range, central Australia. *Journal of Metamorphic Geology*, *19*(4), 373–394. https://doi.org/10.1046/j.0263-4929.2001.00316.x

Buick, I., Storkey, A., & Williams, I. (2008). Timing relationships between pegmatite emplacement, metamorphism and deformation during the intra-plate Alice Springs Orogeny, central Australia. *Journal of Metamorphic Geology*, *26*(9), 915–936. https://doi.org/10.1111/j.1525-1314.2008.00794.x

Buick, I. S., Hand, M., Williams, I. S., Mawby, J., Miller, J. A., & Nicoll, R. S. (2005). Detrital zircon provenance constraints on the evolution of the Harts Range metamorphic complex (central Australia): Links to the centralian superbasin. *Journal of the Geological Society*, *162*(5), 777–787 . https://doi.org/10.1144/0016-764904-044

Burov, E. B., & Watts, A. B. (2006). The long-term strength of continental lithosphere: "Jelly sandwich" or "crème brûlée"? *GSA Today*, *16*(1), 4. https://doi.org/10.1130/1052-5173(2006)016<4:TLTSOC>2.0.CO;2

Camacho, A., & McDougall, I. (2000). Intracratonic, strike-slip partitioned transpression and the formation and exhumation of eclogite facies rocks: An example from the Musgrave block, Central Australia. *Tectonics*, *19*(5), 978–996. https://doi.org/10.1029/1999TC001151

Cartwright, I., & Buick, I. S. (1999). Meteoric fluid flow within Alice Springs age shear zones, Reynolds Range, central Australia. *Journal of Metamorphic Geology*, *17*(4), 397–414. https://doi.org/10.1046/j.1525-1314.1999.00205.x

Cartwright, I., Buick, I. S., Foster, D. A., & Lambert, D. D. (1999). Alice Springs age shear zones from the southeastern Reynolds Range, central Australia. *Australian Journal of Earth Sciences*, *46*(3), 355–363. https://doi.org/10.1046/j.1440-0952.1999.00710.x

Cawood, P. A., Kröner, A., Collins, W. J., Kusky, T. M., Mooney, W. D., & Windley, B. F. (2009). Accretionary orogens through Earth history. *Geological Society, London, Special Publications*, *318*(1), 1–36. https://doi.org/10.1144/SP318.1

Champion, D., Kositcin, N., Huston, D., Mathews, E., & Brown, C. (2009). Geodynamic synthesis of the Phanerozoic of eastern Australia and implications for metallogeny. *Geoscience Australia Record*, *18*, 254.

Coblentz, D. D., Zhou, S., Hillis, R. R., Richardson, R. M., & Sandiford, M. (1998). Topography, boundary forces, and the Indo-Australian intraplate stress field. *Journal of Geophysical Research*, *103*(B1), 919–931. https://doi.org/10.1029/97JB02381

Collins, W., & Shaw, R. (1995). Geochronological constraints on orogenic events in the Arunta inlier: A review. *Precambrian Research*, *71*(1-4), 315–346. https://doi.org/10.1016/0301-9268(94)00067-2

Collins, W., & Teyssier, C. (1989). Crustal scale ductile fault systems in the Arunta inlier, central Australia. *Tectonophysics*, *158*(1-4), 49–66. https://doi.org/10.1016/0040-1951(89)90314-4

Collins, W. J. (2002). Nature of extensional accretionary orogens. *Tectonics*, *21*(4), 1024. https://doi.org/10.1029/2000TC001272

Cunningham, D. (2005). Active intracontinental transpressional mountain building in the mongolian Altai: Defining a new class of orogen. *Earth and Planetary Science Letters*, *240*(2), 436–444. https://doi.org/10.1016/j.epsl.2005.09.013

Cunningham, D. (2013). Mountain building processes in intracontinental oblique deformation belts: Lessons from the Gobi corridor, central Asia. *Journal of Structural Geology*, *46*, 255–282. https://doi.org/10.1016/j.jsg.2012.08.010

Dunlap, W. J., Teyssier, C., McDougall, I., & Baldwin, S. (1995). Thermal and structural evolution of the intracratonic Arltunga Nappe Complex, central Australia. *Tectonics*, *14*(5), 1182–1204. https://doi.org/10.1029/95TC00335

England, P., & McKenzie, D. (1982). A thin viscous sheet model for continental deformation. *Geophysical Journal International*, *70*(2), 295–321. https://doi.org/10.1111/j.1365-246X.1982.tb04969.x

Glen, R. (2013). Refining accretionary orogen models for the Tasmanides of eastern Australia. *Australian Journal of Earth Sciences*, *60*(3), 315–370. https://doi.org/10.1080/08120099.2013.772537

Godin, L., Grujic, D., Law, R. D., & Searle, M. P. (2006). Channel flow, ductile extrusion and exhumation in continental collision zones: An introduction. *Geological Society, London, Special Publications*, *268*(1), 1–23. https://doi.org/10.1144/GSL.SP.2006.268.01.01

Goleby, B. R., Kennett, B. L. N., Wright, C., Shaw, R. D., & Lambeck, K. (1990). Seismic reflection profiling in the Proterozoic Arunta Block, central Australia: Processing for testing models of tectonic evolution. *Tectonophysics*, *173*(1–4), 257–268. https://doi.org/10.1016/0040-1951(90)90222-T

Goleby, B. R., Shaw, R. D., Wright, C., Kennett, B. L. N., & Lambeck, K. (1989). Geophysical evidence for 'thick-skinned' crustal deformation in central Australia. *Nature*, *337*(6205), 325–330. https://doi.org/10.1038/337325a0

Gorczyk, W., Hobbs, B., Gessner, K., & Gerya, T. (2013). Intracratonic geodynamics. *Gondwana Research*, *24*(3–4), 838–848. https://doi.org/10.1016/j.gr.2013.01.006

Gorczyk, W., & Vogt, K. (2015). Tectonics and melting in intra-continental settings. *Gondwana Research*, *27*(1), 196–208. https://doi.org/10.1016/j.gr.2013.09.021

Gray, D., & Foster, D. (2004). Tectonic evolution of the Lachlan orogen, southeast Australia: Historical review, data synthesis and modern perspectives. *Australian Journal of Earth Sciences*, *51*(6), 773–817. https://doi.org/10.1111/j.1400-0952.2004.01092.x

Haines, P. W., Hand, M., & Sandiford, M. (2001). Palaeozoic synorogenic sedimentation in central and northern Australia: A review of distribution and timing with implications for the evolution of intra-continental orogens. *Australian Journal of Earth Sciences*, *48*(6), 911–928. https://doi.org/10.1046/j.1440-0952.2001.00909.x

Hand, M., Mawby, J., Kinny, P., & Foden, J. (1999). U–Pb ages from the Harts Range, central Australia: Evidence for early Ordovician extension and constraints on Carboniferous metamorphism. *Journal of the Geological Society*, *156*(4), 715–730. https://doi.org/10.1144/gsjgs.156.4.0715

Hand, M., & Sandiford, M. (1999). Intraplate deformation in central Australia, the link between subsidence and fault reactivation. *Tectonophysics*, *305*(1-3), 121–140. https://doi.org/10.1016/S0040-1951(99)00009-8

Handy, M. R., & Brun, J. P. (2004). Seismicity, structure and strength of the continental lithosphere. *Earth and Planetary Science Letters*, *223*(3–4), 427–441. https://doi.org/10.1016/j.epsl.2004.04.021

Heron, P. J., & Pysklywec, R. N. (2016). Inherited structure and coupled crust-mantle lithosphere evolution: Numerical models of Central Australia. *Geophysical Research Letters*, *43*, 4962–4970. https://doi.org/10.1002/2016GL068562

Heron, P. J., Pysklywec, R. N., & Stephenson, R. (2016). Lasting mantle scars lead to perennial plate tectonics. *Nature Communications*, *7*, 11834. https://doi.org/10.1038/ncomms11834

Houseman, G., Barr, T., & Evans, L. (2008). *Basil: stress and deformation in a viscous material. Microdynamics simulation* (pp. 139–154). Berlin: Springer-Verlag.

Houseman, G., & England, P. (1986). Finite strain calculations of continental deformation: 1. Method and general results for convergent zones. *Journal of Geophysical Research*, *91*(B3), 3651–3663. https://doi.org/10.1029/JB091iB03p03651

Houseman, G., & England, P. (1993). Crustal thickening versus lateral expulsion in the Indian-Asian continental collision. *Journal of Geophysical Research*, *98*(B7), 12,233–12,249. https://doi.org/10.1029/93JB00443

Hurd, O., & Zoback, M. D. (2012). Intraplate earthquakes, regional stresses and faults mechanics in the central and eastern U.S. and Southern Canada. *Tectonophysics*, *581*, 182–192. https://doi.org/10.1016/j.tecto.2012.04.002

Karato, S. I., Paterson, M. S., & FitzGerald, J. D. (1986). Rheology of synthetic olivine aggregates: Influence of grain size and water. *Journal of Geophysical Research*, *91*(B8), 8151–8176. https://doi.org/10.1029/JB091iB08p08151

Klootwijk, C. (2010). Australia's controversial Middle-Late Palaeozoic pole path and Gondwana–Laurasia interaction. *Palaeoworld*, *19*(1-2), 174–185. https://doi.org/10.1016/j.palwor.2009.12.004

Klootwijk, C. (2013). Middle–late Paleozoic Australia-Asia convergence and tectonic extrusion of Australia. *Gondwana Research*, *24*(1), 5–54. https://doi.org/10.1016/j.gr.2012.10.007

Korsch, R. J., Goleby, B. R., Leven, J. H., & Drummond, B. J. (1998). Crustal architecture of Central Australia based on deep seismic reflection profiling. *Tectonophysics*, *288*(1–4), 57–69. https://doi.org/10.1016/S0040-1951(97)00283-7

Kröner, A. (1977). Precambrian mobile belts of southern and eastern Africa—Ancient sutures or sites of ensialic mobility? A case for crustal evolution towards plate tectonics. *Tectonophysics*, *40*(1–2), 101–135. https://doi.org/10.1016/0040-1951(77)90031-2

Kröner, U., Roscher, M., & Romer, R. L. (2016). Ancient plate kinematics derived from the deformation pattern of continental crust: Paleo-and Neo-Tethys opening coeval with prolonged Gondwana–Laurussia convergence. *Tectonophysics*, *681*, 220–233. https://doi.org/10.1016/j.tecto.2016.03.034

Kusznir, N. J., & Park, R. G. (1987). The extensional strength of the continental lithosphere: Its dependence on geothermal gradient, and crustal composition and thickness. *Geological Society, London, Special Publications*, *28*(1), 35–52. https://doi.org/10.1144/GSL.SP.1987.028.01.04

Livaccari, R. F. (1991). Role of crustal thickening and extensional collapse in the tectonic evolution of the Sevier-Laramide orogeny, western United States. *Geology*, *19*(11), 1104–1107. https://doi.org/10.1130/0091-7613(1991)019<1104:ROCTAE>2.3.CO;2

Maidment, D. (2005). *Palaeozoic high-grade metamorphism within the Centralian Superbasin, Harts Range region, central Australia* (Unpublished doctoral dissertation). Canberra, Australia: Australian National University.

Maidment, D., Hand, M., & Williams, I. (2013). High–grade metamorphism of sedimentary rocks during Palaeozoic rift basin formation in central Australia. *Gondwana Research*, *24*(3-4), 865–885. https://doi.org/10.1016/j.gr.2012.12.020

Marshak, S., Karlstrom, K., & Timmons, J. M. (2000). Inversion of Proterozoic extensional faults: An explanation for the pattern of Laramide and Ancestral Rockies intracratonic deformation, United States. *Geology*, *28*(8), 735–738. https://doi.org/10.1130/0091-7613(2000)28<735:IOPEFA>2.0.CO;2

Mawby, J., Hand, M., & Foden, J. (1999). Sm–Nd evidence for high–grade ordovician metamorphism in the Arunta block, central Australia. *Journal of Metamorphic Geology*, *17*(6), 653–668. https://doi.org/10.1046/j.1525-1314.1999.00224.x

McLaren, S., Sandiford, M., Dunlap, W. J., Scrimgeour, I., Close, D., & Edgoose, C. (2009). Distribution of Palaeozoic reworking in the western Arunta region and northwestern Amadeus basin from 40ar/39ar thermochronology: Implications for the evolution of intracratonic basins. *Basin Research*, *21*(3), 315–334. https://doi.org/10.1111/j.1365-2117.2008.00385.x

Meng, Q. R., & Zhang, G. W. (2000). Geologic framework and tectonic evolution of the Qinling orogen, central China. *Tectonophysics*, *323*(3-4), 183–196. https://doi.org/10.1016/S0040-1951(00)00106-2

Molnar, P., & Dayem, K. E. (2010). Major intracontinental strike-slip faults and contrasts in lithospheric strength. *Geosphere*, *6*(4), 444–467. https://doi.org/10.1130/GES00519.1

Molnar, P., & Tapponnier, P. (1975). Cenozoic tectonics of Asia: Effects of a continental collision. *Science*, *189*(4201), 419–426. https://doi.org/10.1126/science.189.4201.419

Mory, A. & Beere, G. (1988). *Geology of the onshore Bonaparte and Ord basins in western Australia*. *Geological Survey Western Australia*, (Bulletin 134). Perth, WA: Geological Survey of Western Australia.

Myers, J. S., Shaw, R. D., & Tyler, I. M. (1996). Tectonic evolution of Proterozoic Australia. *Tectonics*, *15*(6), 1431–1446. https://doi.org/10.1029/96TC02356

Neil, E. A., & Houseman, G. A. (1999). Rayleigh–Taylor instability of the upper mantle and its role in intraplate orogeny. *Geophysical Journal International*, *138*(1), 89–107. https://doi.org/10.1046/j.1365-246x.1999.00841.x

Neves, S. P. (2003). Proterozoic history of the Borborema province (NE Brazil): Correlations with neighboring cratons and Pan-African belts and implications for the evolution of western Gondwana. *Tectonics*, *22*(4), 1031. https://doi.org/10.1029/2001TC001352

Perry, H. K. C., Mareschal, J. C., & Jaupart, C. (2006). Variations of strength and localized deformation in cratons: The 1.9 Ga Kapuskasing uplift, Superior Province, Canada. *Earth and Planetary Science Letters*, *249*(3–4), 216–228. https://doi.org/10.1016/j.epsl.2006.07.013

Powell, C. M. (1984). Terminal fold–belt deformation: Relationship of mid–Carboniferous megakinks in the Tasman fold belt to coeval thrusts in cratonic Australia. *Geology*, *12*(9), 546–549. https://doi.org/10.1130/0091-7613(1984)12<546:TFDROM>2.0.CO;2

Pysklywec, R. N., & Beaumont, C. (2004). Intraplate tectonics: Feedback between radioactive thermal weakening and crustal deformation driven by mantle lithosphere instabilities. *Earth and Planetary Science Letters*, *221*(1–4), 275–292. https://doi.org/10.1016/S0012-821X(04)00098-6

Raimondo, T., Clark, C., Hand, M., Cliff, J., & Anczkiewicz, R. (2013). A simple mechanism for mid-crustal shear zones to record surface-derived fluid signatures. *Geology*, *41*(6), 711–714. https://doi.org/10.1130/G34043.1

Raimondo, T., Clark, C., Hand, M., Cliff, J., & Harris, C. (2012). High-resolution geochemical record of fluid-rock interaction in a mid-crustal shear zone: A comparative study of major element and oxygen isotope transport in garnet. *Journal of Metamorphic Geology*, *30*(3), 255–280. https://doi.org/10.1111/j.1525-1314.2011.00966.x

Raimondo, T., Clark, C., Hand, M., & Faure, K. (2011). Assessing the geochemical and tectonic impacts of fluid-rock interaction in mid-crustal shear zones: A case study from the intracontinental Alice Springs orogen, central Australia. *Journal of Metamorphic Geology*, *29*(8), 821–850. https://doi.org/10.1111/j.1525-1314.2011.00944.x

Raimondo, T., Collins, A. S., Hand, M., Walker-Hallam, A., Smithies, R. H., Evins, P. M., & Howard, H. M. (2010). The anatomy of a deep intra-continental orogen. *Tectonics*, *29*, TC4024. https://doi.org/10.1029/2009TC002504

Raimondo, T., Hand, M., & Collins, W. J. (2014). Compressional intracontinental orogens: Ancient and modern perspectives. *Earth-Science Reviews*, *130*, 128–153. https://doi.org/10.1016/j.earscirev.2013.11.009

Ramdani, F. (1998). Geodynamic implications of intermediate-depth earthquakes and volcanism in the intraplate Atlas mountains (Morocco). *Physics of the Earth and Planetary Interiors*, *108*(3), 245–260. https://doi.org/10.1016/S0031-9201(98)00106-X

Ranalli, G., & Murphy, D. C. (1987). Rheological stratification of the lithosphere. *Tectonophysics*, *132*(4), 281–295. https://doi.org/10.1016/0040-1951(87)90348-9

Regenauer-Lieb, K., Veveakis, M., Poulet, T., Paesold, M., Rosenbaum, G., Weinberg, R. F., & Karrech, A. (2015). Multiscale, multiphysics geomechanics for geodynamics applied to buckling instabilities in the middle of the Australian craton. *Philosophical Magazine*, *95*(28–30), 3055–3077. https://doi.org/10.1080/14786435.2015.1066517

Rey, P. F., Mondy, L., Duclaux, G., Teyssier, C., Whitney, D. L., Bocher, M., & Prigent, C. (2017). The origin of contractional structures in extensional gneiss domes. *Geology*, *45*(3), 263–266. https://doi.org/10.1130/G38595.1

Roberts, E. A., & Houseman, G. A. (2001). Geodynamics of central Australia during the intraplate Alice Springs Orogeny: Thin viscous sheet models. *Geological Society, London, Special Publications*, *184*(1), 139–164. https://doi.org/10.1144/GSL.SP.2001.184.01.08

Romine, K., Southgate, P., Kennard, J., & Jackson, M. (1994). *The Ordovician to Silurian phase of the Canning basin*, *The sedimentary basins of Western Australia* (pp. 677–696). WA: Structure and sequence evolution.

Sandiford, M., & Hand, M. (1998). Controls on the locus of intraplate deformation in central Australia. *Earth and Planetary Science Letters*, *162*(1-4), 97–110. https://doi.org/10.1016/S0012-821X(98)00159-9

Sandiford, M., Hand, M., & McLaren, S. (2001). Tectonic feedback, intraplate orogeny and the geochemical structure of the crust: A central Australian perspective. *Geological Society, London, Special Publications*, *184*(1), 195–218. https://doi.org/10.1144/GSL.SP.2001.184.01.10

Scrimgeour, I. R. (2013). Aileron Province. In M. Ahmad & T. J. Munson (Eds.), *Geology and mineral resources of the Northern Territory*, *Northern Territory Geological Survey, Special Publication* (Vol. 5, pp. 12:1–12:74). Darwin, NT: Northern Territory Geological Survey.

Shaw, R., Etheridge, M., & Lambeck, K. (1991). Development of the late–Proterozoic to mid-Paleozoic intracratonic Amadeus basin in central Australia: A key to understanding tectonic forces in plate interiors. *Tectonics*, *10*(4), 688–721. https://doi.org/10.1029/90TC02417

Shaw, R., Wellman, P., Gunn, P., Whitaker, A., Tarlowski, C., & Morse, M. (1995). Australian crustal elements map. *AGSO Research Newsletter*, *23*, 1–3.

Teixell, A., Arboleya, M.-L., Julivert, M., & Charroud, M. (2003). Tectonic shortening and topography in the central High Atlas (Morocco). *Tectonics*, *22*(5), 1051. https://doi.org/10.1029/2002TC001460

Teyssier, C. (1985). A crustal thrust system in an intracratonic tectonic environment. *Journal of Structural Geology*, *7*(6), 689–700. https://doi.org/10.1016/0191-8141(85)90144-0

Thomas, W. A., & Powell, C. A. (2017). Necessary conditions for the intraplate seismic zones in North America. *Tectonics*, *36*, 2903–2917. https://doi.org/10.1002/2017TC004502

Tommasi, A., Vauchez, A., & Daudré, B. (1995). Initiation and propagation of shear zones in a heterogeneous continental lithosphere. *Journal of Geophysical Research*, *100*(B11), 22,083–22,101. https://doi.org/10.1029/95JB02042

Tucker, N. M., Hand, M., & Payne, J. L. (2015). A rift–related origin for regional medium–pressure, high–temperature metamorphism. *Earth and Planetary Science Letters*, *421*, 75–88. https://doi.org/10.1016/j.epsl.2015.04.003

Walter, M. R., Veevers, J. J., Calver, C. R., & Grey, K. (1995). Neoproterozoic stratigraphy of the centralian superbasin, Australia. *Precambrian Research*, *73*(1–4), 173–195. https://doi.org/10.1016/0301-9268(94)00077-5

Webby, B. D. (1978). History of the Ordovician continental platform shelf margin of Australia. *Journal of the Geological Society of Australia*, *25*(1–2), 41–63. https://doi.org/10.1080/00167617808729013

Weisheit, A., Reno, B. L., Beyer, E. E., Whelan, J. A., McGloin, M., (2016). Multiply reactivated crustal–scale structures and a long– lived counter–clockwise P–T path: New insights into the 1.5 billion year tectonothermal evolution of the eastern Arunta region, central Australia. Annual Geoscience Exploration Seminar (AGES) Proceedings, Alice Springs, Northern Territory (pp. 56–52). Darwin, NT: Northern Territory Geological Survey.

Whitney, D. L., Teyssier, C., & Vanderhaege, O. (2004). Gneiss domes and crustal flow. In D. L. Whitney, C. Teyssier, & C. S. Siddoway (Eds.), *Gneiss domes in orogeny*, *Special Paper* (Vol. 380, pp. 15–13). America: Geological Society.

Wright, C., Goleby, B. R., Collins, C. D. N., Korsch, R. J., Barton, T., Greenhalgh, S. A., & Sugiharto, S. (1990). Deep seismic profiling in central Australia. *Tectonophysics*, *173*(1–4), 247–256. https://doi.org/10.1016/0040-1951(90)90221-S

Zoback, M. L., Zoback, M. D., Adams, J., Assumpcao, M., Bell, S., Bergman, E. A., Blumling, P., et al. (1989). Global patterns of tectonic stress. *Nature*, *341*(6240), 291–298. https://doi.org/10.1038/341291a0